AIMS Materials Science, 3(3): 686-721.
DOI: 10.3934/matersci.2016.3.686
Received: 13 May 2016
Accepted: 12 June 2016
Published: 14 June 2016

http://www.aimspress.com/journal/Materials

Research article

Penetration resistance and ballistic-impact behavior of $Ti/TiAl_3$ metal/intermetallic laminated composites (MILCs): A computational investigation

Mica Grujicic, Jennifer S. Snipes, and S. Ramaswami *

Department of Mechanical Engineering, Clemson University, Clemson SC 29634, USA

*** Correspondence:** Email:gmica@clemson.edu; Tel: +1-864-656-5639; Fax: +1-864-656-4435.

Abstract: A comprehensive computational engineering analysis is carried out in order to assess suitability of the $Ti/TiAl_3$ metal/intermetallic laminated composites (MILCs) for use in both structural and add-on armor applications. This class of composite materials consists of alternating sub-millimeter thick layers of Ti (the ductile and tough constituent) and $TiAl_3$ (the stiff and hard constituent). In recent years, this class of materials has been investigated for potential use in light-armor applications as a replacement for the traditional metallic or polymer-matrix composite materials. Within the computational analysis, an account is given to differing functional requirements for candidate materials when used in structural and add-on ballistic armor. The analysis employed is of a transient, nonlinear-dynamics, finite-element character, and the problem investigated involves normal impact (i.e. under zero obliquity angle) of a $Ti/TiAl_3$ MILC target plate, over a range of incident velocities, by a fragment simulating projectile (FSP). This type of analysis can provide more direct information regarding the ballistic limit of the subject armor material, as well as help with the identification of the nature and the efficacy of various FSP material-deformation/erosion and kinetic-energy absorption/dissipation phenomena and processes. The results obtained clearly revealed that $Ti/TiAl_3$ MILCs are more suitable for use in add-on ballistic, than in structural armor applications.

Keywords: $Ti/TiAl_3$ metal/intermetallic laminated composites; ballistic impact; penetration

1. Introduction

The present work addresses the problem of penetration resistance and ballistic-impact behavior of Ti/$TiAl_3$ metal/intermetallic laminated composites (MILCs), a class of materials being considered for use in multi-layer/multi-functional light-armor applications. Consequently, the concepts most relevant to this study are: (a) multi-layer/multi-functional armor; (b) the basics of Ti/$TiAl_3$ MILCs; (c) previous experimental work pertaining to the ballistic-impact performance of Ti/$TiAl_3$ MILCs; and (d) prior computational modeling and simulation work dealing with the ballistic-impact behavior and penetration resistance of Ti/$TiAl_3$ MILCs. Each of these concepts is briefly described in this section.

1.1. Multi-Layer/Multi-Functional Armor

Armor systems for (battlefield and tactical) military-vehicles were traditionally made of metallic materials such as steel and aluminum. While their superior combination of strength and toughness makes them more suitable in structural applications, these materials could offer adequate ballistic/blast protection, if used in components having a sufficiently high areal density [1,2]. However, doing so typically leads to excessively heavy vehicles having reduced fuel efficiency, transportability/deployability and mobility, and often greater susceptibility to mechanical/structural in-service failure. Therefore, research is underway to help engineer light-weight, highly mobile, transportable and lethal battlefield and tactical vehicles. One goal of such research is to develop novel light-weight materials and armor architectures having superior ballistic penetration performance and blast survivability.

Four recent approaches to develop light-weight high-performance armor systems are particularly noteworthy: (a) *monolithic ceramic armor* [3]—the superior combination of low density, high hardness, high stiffness, high (compressive) strength and good thermal stability of these materials is used to advantage; (b) *ceramic matrix composites* [4]—to address the problem of limited toughness (high brittleness) of monolithic ceramic armor systems, whiskers or fiber reinforcements within the ceramic matrix are used; (c) *polymer-based composite armor systems* [5,6]—the ballistic mass efficiency of the armor is increased using continuous fiber-reinforced polymer-matrix composites. While such armor systems generally provide adequate ballistic protection against the so-called "non-armor piercing (non-AP)" projectiles, they are readily defeated by the so-called "armor piercing (AP)" projectiles; and (d) *hybrid multi-layer/multi-functional laminated armor systems* [7].

As shown in the schematic of in Figure 1, a prototypical architecture of this type of armor system consists of a number of layers, each of which serves a specific purpose, while the combinations/interactions of layers provide role-sharing and multi-functionality. The main layers appearing in a prototypical multi-functional armor include: (i) a thin, outermost, polymer-matrix composite face sheet the main role of which is to protect the underlying ceramic layer from accidental damage and/or environmental attack; (ii) a ceramic strike-face layer, typically consisting of individual tiles, the primary function of which is to erode and/or break up the projectile upon impact; (iii) a thin (typically Ethylene Propylene-based Diene Monomer, EPDM, rubber, polyurethane/polyurea or acrylic) adhesive layer that bonds the ceramic tiles to the underlying back-up armor plates. In addition, this layer often mechanically isolates the impacted tile from the surrounding tiles, improving the multi-hit capability of the armor system; (iv) a relatively thicker backing plate, typically made of either light metallic or polymer-based composite materials. Its main role is to limit ceramic-tile back-face bending deflection, to absorb the kinetic energy of (and

preferably arrest) the projectile and ceramic-tile fragments, and to provide additional structural stiffness/strength to the vehicle-frame/body. There has been a suggestion to consider MILCs in the construction of this layer [8]. It is the case of the Ti/$TiAl_3$ MILC backing plate that is considered in the present study; and (v) the innermost "spall" layer, typically made of a phenolic resin-based material. The main function of this layer is to capture armor and projectile fragments/debris and to act as a fire retardant. In order to impart additional non-structural/non-ballistic (e.g. electro-magnetic ground planes, signature control, etc.) functions to the multi-functional armor, additional layers may be incorporated [9].

While the present study considers the ballistic behavior of the isolated Ti/$TiAl_3$ MILC backing plates, the performance of these plates is judged with respect to their potential role in a multi-functional/multi-layer armor system.

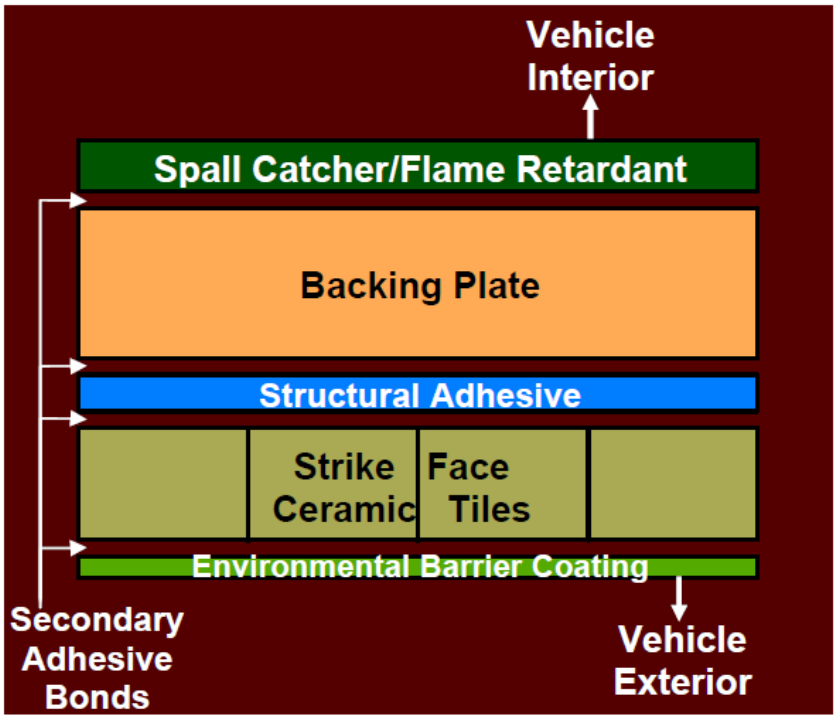

Figure 1. Architecture of the multi-functional composite armor (schematic).

1.2. The Basics of Ti/$TiAl_3$ MILCs

Ti/$TiAl_3$ MILCs consist of alternating layers of Ti (the ductile and tough phase) and $TiAl_3$ (the stiff and hard phase), with each layer less than one millimeter thick [10–15]. A relatively new class of structural (and, potentially, ballistic-protection) materials, they are generally fabricated using a one-step process within which commercially-available elemental Ti and Al foils (of desired thicknesses) are stacked and (melt) reactively sintered by subjecting them to elevated temperatures and pressures (in open-air). To ensure that no residual aluminum is present (or that the residual aluminum volume fraction is in a given range) and that the volume fractions of the two phases are within the target ranges in the as-fabricated MILC, initial thicknesses of the Ti and Al foils are selected accordingly. This MILC fabrication process offers a number of advantages: (a) a high level of flexibility with respect to the selection of the foil materials and thicknesses; (b) it enables tailoring

of the final material properties through the employment of the so-called "material-by-design" approach within which required foil materials thicknesses and layering sequence are determined/identified; (c) the process can be readily scaled up for the commercial/industrial use; (d) the process is economically attractive since it relies on the use of commercially available materials/foils and is conducted under modest temperature (typically <1000 K), modest pressure (typically <4 MPa) and open-air (special vacuum/inert gas chambers are not required) conditions; (e) since the initial materials (i.e. the metallic foils) are fairly ductile, the process can be used to fabricate near net shape components of complex-geometry containing curved surfaces, cavities, pathways, etc.; and (f) in regard to the Ti/Al system, the MILC fabrication process is ideal since, between the three possible Titanium Aluminides (i.e. Ti_3Al, TiAl and $TiAl_3$), it produces, for the thermodynamics and kinetics reasons, $TiAl_3$, the phase with the superior combination of high Young's modulus (216 GPa), high oxidation resistance and low mass density (3.3 g/cm^3).

Experimental studies [10] have shown that $Ti/TiAl_3$ MILCs possess a superior combination of specific (i.e. mass-density normalized) stiffness, hardness/compressive strength and fracture toughness. These observations have been reiterated by the (log-log) material selection charts displayed in Figures 2(a)-(b). In Figure 2(a) the specific compressive strength (the *y*-axis) is plotted against the specific stiffness (the *x*-axis), while in Figure 2(b) the specific fracture toughness (the *y*-axis) is plotted against the specific stiffness (the *x*-axis). Examination of these figures reveals that: (a) the specific stiffness of $Ti/TiAl_3$ MILCs is superior to that found in most metallic materials (e.g. steels, titanium alloys, nickel super-alloys, aluminum alloys and titanium-based inter-metallics), except for beryllium alloys; (b) the specific stiffness of $Ti/TiAl_3$ MILCs is comparable to, but somewhat lower than that found in technical monolithic-ceramics (e.g. SiC, B_4C, Al_2O_3 and diamond); (c) the specific compressive strength and toughness of $Ti/TiAl_3$ MILCs is comparable to, or better than, that found in most metallic and technical monolithic-ceramic materials; and (d) the combination of the specific stiffness, compressive strength and fracture toughness found in these materials is on par with, or better than, that found in most laminated metal-matrix composites (at the comparable level of the ductile phase).

$Ti/TiAl_3$ MILCs are being considered as potential replacements for metallic and polymer-matrix composite materials in the backing plates of multi-layer armor. Since a main role of the backing plate is to provide stiff back-support to the ceramic strike face (so that it does not excessively bend), the data presented in Figures 2(a)-(b) and the discussion of these charts suggest that $Ti/TiAl_3$ MILCs are respectable candidate materials for use in these applications. However, the backing plate has another, very important role: to efficiently absorb and dissipate the kinetic energy of the incoming projectile (without being penetrated). Furthermore, continued erosion of the projectile by the backing plate is desirable. The specific compressive strength and the specific fracture toughness data presented in Figures 2(a)-(b) suggest that $Ti/TiAl_3$ MILCs could be effective in absorbing the projectile kinetic energy and in eroding the projectile. However, to fully establish the ballistic-impact performance of these materials, direct experimental and/or computational investigations have to be carried out.

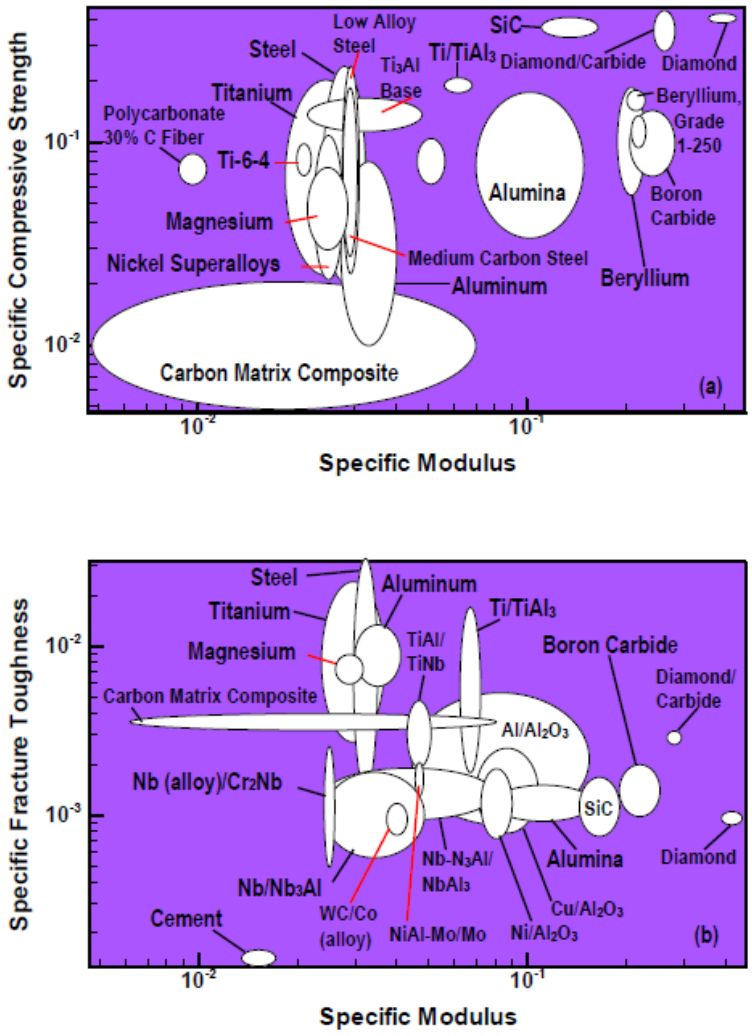

Figure 2. Material selection charts: (a) Specific compressive strength; and (b) specific fracture toughness vs. specific Young's modulus.

1.3. Previous Experimental Work Pertaining to the Ballistic-Impact Performance of Ti/TiAl$_3$ MILCs

There appears to be only one published report of an experimental study of the ballistic performance of Ti/TiAl$_3$ MILCs [16]. That study concerned the ballistic behavior of a 20-mm-thick Ti/TiAl$_3$ MILC target plate under normal (i.e. zero obliquity angle) impact at a velocity of 900 m/s. The target plate consisted of 18 equal-thickness Ti and 17 equal-thickness TiAl$_3$ layers (the volume fraction of the ductile Ti phase was approximately 20%), and had a mass density of 3.5 g/cm^3. The impactor was made of tungsten heavy alloy (chemical composition: W 93 wt%, Fe+Co the remainder), and had the shape of a solid circular cylinder (diameter = 6.15 mm, length = 23 mm, mass = 10 grams) with a hemispherical tip. For a ballistic limit comparable to that of an armor-grade steel target plate, the Ti/TiAl$_3$ MILC target plate was found to have nearly one half of the steel areal density. This outstanding ballistic performance of the MILC target plate was attributed to: (a) extensive plastic stretching of the ductile Ti phase; (b) extensive fragmentation of the brittle TiAl$_3$ phase; (c) extensive delamination along the Ti/TiAl$_3$ interfaces; (d) efficient TiAl$_3$-crack bridging by the Ti phase; and (e) the ability of hard TiAl$_3$ laminae to continually blunt and erode the advancing

projectile.

1.4. Prior Computational Modeling and Simulation Work Dealing with the Ballistic-Impact Behavior and Penetration Resistance of Ti/TiAl$_3$ MILCs

Most of the published computational modeling and simulation studies dealing with the Ti/TiAl$_3$ MILCs is concerned with their fabrication and with relating the fabrication-process parameters to the resulting material microstructure and (quasi-static) mechanical properties (not the subject of the present work). Apparently only one study concerned with modeling and simulation of the ballistic-impact performance of Ti/TiAl$_3$ MILCs has been published, by Zelepugin et al. [17], who employed an axisymmetric finite element analysis, under adiabatic thermal conditions, to simulate the ballistic-impact problem investigated experimentally by Harach [16]. Because critical details of the finite element analysis, such as the formulation and the parameterization of the material constitutive models and contact algorithms, were not revealed by Zelepugin et al. [17], the physical soundness of the analysis cannot be assessed and the results reported could not be reproduced. The key finding of their analysis was that the maximum ballistic-penetration performance of the Ti/TiAl$_3$ MILCs under normal 900 m/s impact is obtained for an optimal volume fraction of the ductile phase.

Clearly, a comprehensive computational (as well as an experimental) investigation of the ballistic-impact performance of Ti/TiAl$_3$ MILCs is needed in order to assess their potential for use, as backing plates, in multi-layer light-weight armor systems.

1.5. Main Objective

The main objective of this study is to develop a transient, nonlinear-dynamics, finite-element model of normal impact (i.e. at zero obliquity angle) of a Ti/TiAl$_3$ MILC target plate by a fragment simulating projectile (FSP), over a range of incident velocities. The main emphasis within the finite-element model development is on identifying the nature and the efficacy of various FSP material-deformation/erosion and kinetic-energy absorption/dissipation phenomena and processes. The computational model and analysis will be validated by comparing the results with the experimental data of Harach [16]. In addition, the results will be used to pass a more definite judgment regarding the suitability of the Ti/TiAl$_3$ MILCs, as backing-plate materials, in multi-layer light-weight armor systems.

1.6. Paper Organization

The computational analysis used in this study is summarized in Section 2. Details of the formulation, parameterization and validation of the material models employed are given in Section 3. The key results of the present investigation are presented and discussed in Section 4, while the main conclusions of this study are summarized in Section 5.

2. Problem Definition and Computational Procedure

In this section, a brief description is provided of the problem related to the normal impact, at different incident velocities, of a Ti/TiAl$_3$ MILC target plate by an FSP. A brief description is also

provided of the transient, nonlinear dynamics, finite-element analysis (FEA) used to model this problem.

2.1. Problem Definition

This computational study concerns the normal (i.e. zero-obliquity angle) impact of a .50 caliber FSP onto a 20 mm thick Ti/$TiAl_3$ MILC target plate. The FSP has a Solid Right Circular Cylindrical (SRCC) shape and is made of tungsten heavy-alloy. The target plate consists of 18 Ti layers (each ca. 0.223 mm thick) and 17 $TiAl_3$ layers (each 0.94 mm thick). These thicknesses of the Ti and $TiAl_3$ layers can be produced from the commercially-available Al- and Ti-foil thicknesses used in Ref. [16] as well as by employing the foil stacking and complex thermo-mechanical annealing procedure which involved temperatures as high as 1023 K. The FSP incident velocity was varied in the 500 to 1500 m/s range. Two key questions to be answered are: (a) whether the present computational analysis can provide realistic predictions (i.e. predictions which are in agreement with the experimental findings reported in Ref. [16]) regarding the nature and the extent of damage sustained by the Ti/$TiAl_3$ MILC target plate during the impact; and (b) whether the present approach can provide additional insight into the nature and the efficacy of different FSP material-deformation/erosion and kinetic-energy absorption/dissipation mechanisms.

2.2. Finite-Element Analysis

The FEA employed requires specification of the following: (a) geometrical model; (b) meshed model; (c) computational algorithm; (d) initial conditions; (e) boundary conditions; (f) contact interactions; (g) material models; and (h) computational tool. These aspects are briefly overviewed in the remainder of this sub-section.

2.2.1. Geometrical Model

The (Lagrangian) computational domain comprises a .25 caliber SRCC Tungsten FSP and a 20 mm thick multi-layer Ti/$TiAl_3$ MILC target plate the internal architecture of which has been described. Since: (a) all the materials analyzed are assumed to be continuum and isotropic; (b) the FSP impacts the target-plate normally; and (c) the FSP/target-plate interaction is unaffected by stress waves reflected from the target-plate lateral faces, the model possesses circular symmetry with the FSP-axis acting as the axis of rotational symmetry. Although a two-dimensional FEA appears appropriate, ABAQUS/Explicit, (the general-purpose FEA program used [18]) lacks important aspects of the contact algorithm within its two-dimensional formulations. For this reason, a three-dimensional FEA is employed, but only of a 5° sector, while applying the appropriate symmetry boundary conditions across the (0° and 5°) radial faces of the segment. The complete 360° geometrical model employed (obtained by replicating the original 5° sector 360/5 = 72 times and rotating each new replica by an additional 5° about the vertical *z*-axis, the axis of symmetry) is depicted in Figure 3(a). For improved clarity, thinner Ti laminae and thicker $TiAl_3$ laminae are colored differently.

Since the computational analysis had to be validated against the experimental results of Harach [16], in which a (6.15 mm diameter, 23 mm length) SRCC with a hemispherical cap was used, an additional geometrical model, Figure 3(b), had to be constructed and used. The reason that a

flat-head SRCC FSP was used in the present work is that this projectile shape is generally considered to be more representative of a typical high-velocity fragment.

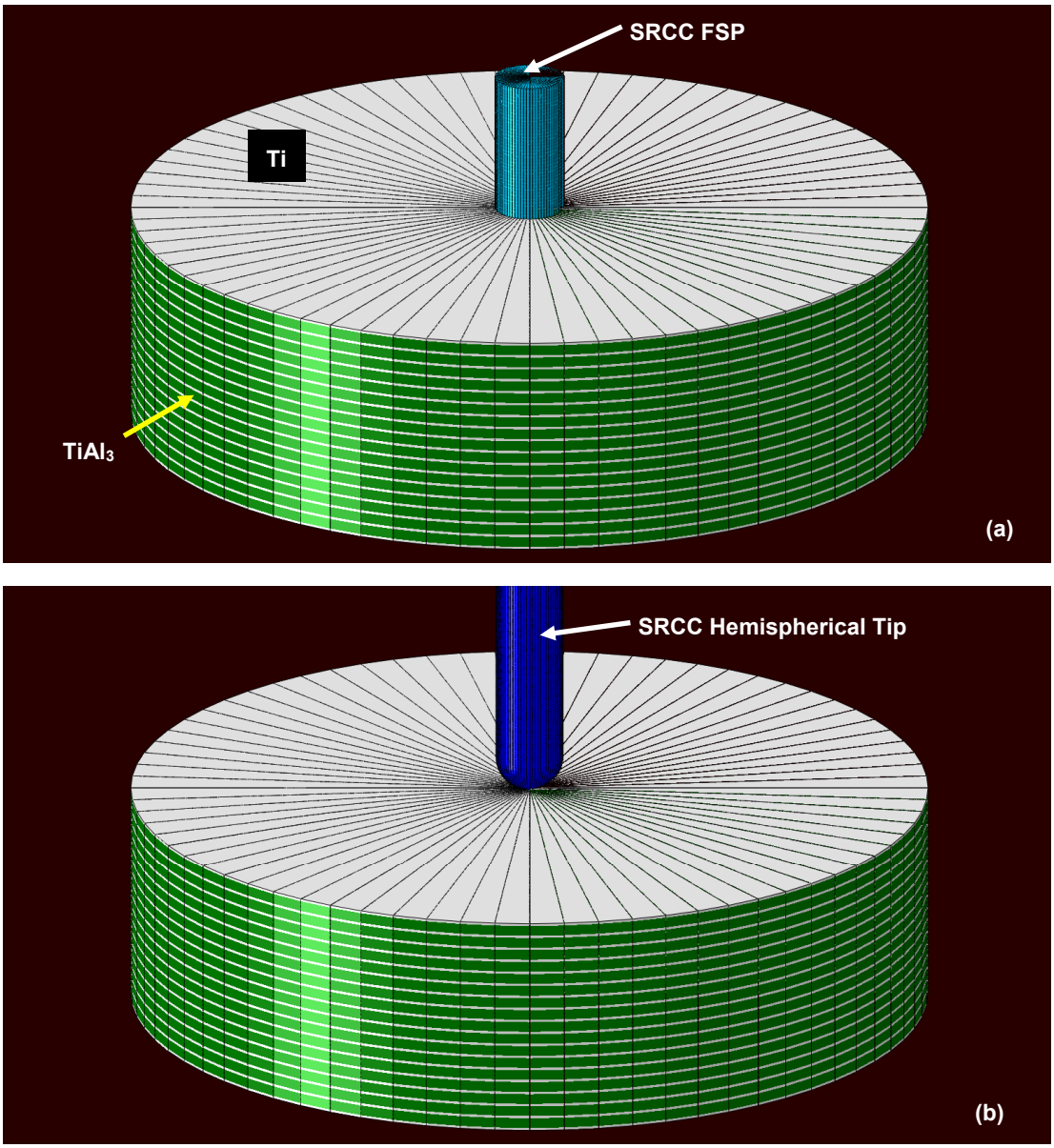

Figure 3. Geometrical models of Ti/$TiAl_3$ MILC target-plate and projectiles: (a) SRCC Tungsten FSP; and (b) SRCC Tungsten projectile, containing a hemispherical tip.

In addition to the FSP/projectile and the MILC target plate, a square witness plate having a footprint larger than that of the target plate was placed 30 cm away from the back-face of the target plate. The witness plate was modeled as a rigid single-element shell structure and its role was to detect the generation and propulsion of the target-plate back-face spall fragments. In other words, the witness plate remains stationary (no gravity loading applied), unless it is impacted by one or more spall fragments.

2.2.2. Meshed Model

The FSP and target plate are meshed using eight-node first-order reduced-integration continuum finite elements, except for the regions adjacent to the axis of symmetry. The latter regions are meshed using six-node first-order reduced-integration continuum finite elements. In addition, finite elements adjacent to the circumferential boundary of the target-plate are converted into the eight-node "infinite" elements to prevent reflection of the stress waves from this boundary. Doing so ensures that the computational analysis depicts the experimental test condition employed by Harach [16] more accurately. That is in Ref. [16] the lateral dimensions of the target plate are significantly larger than the ones used in the present work. For this reason, in Ref. [16], the FSP/target-plate interactions were unaffected by wave reflection from the target-plate lateral faces. On the other hand, should reflected waves be allowed to be generated in the present analysis, they could significantly affect/alter the outcome of the FSP/target-plate interaction. In the majority of the analyses carried out, the FSP and target-plate contained 800 and 4000–4500 elements, respectively. Figure 4(a) shows a close-up view of the FSP/target-plate meshed model for a single 5° sector, near the rotational axis, along with the Cartesian coordinate system employed throughout the analysis. Figure 4(b) depicts the corresponding meshed model for the projectile/target-plate case.

At the shared edges between adjacent lamellae, eight-node (and six-node, in the region adjacent to the axis of rotation), three-dimensional, traction/separation cohesive-zone finite elements are placed in order to represent inter-lamellar $Ti/TiAl_3$ boundaries. The number of cohesive-zone elements is affected by the number of continuum elements, since the former elements share nodes with the adjacent continuum elements. It should be noted that the traction-separation cohesive-zone elements are a special class of finite elements which enable modeling of the normal- and/or shear-traction induced interfacial decohesion. These elements are not visible in Figures 4(a)-(b), since no decohesion is present in the initial configuration.

2.2.3. Computational Algorithm

All the calculations use a transient, displacement-based, purely-Lagrangian, conditionally-stable, dynamic-explicit finite-element algorithm. While the FSP/target-plate interactions can result in substantial local-temperature increase, adiabatic conditions were assumed, i.e. the temperature was assumed to increase only at the location where the FSP kinetic-energy is dissipated in the form of heat. This assumption is justified by the fact that the FSP/target-plate interactions can result in substantial local-temperature increase and the characteristic-times of these interactions are significantly shorter than the FSP/target-plate thermal-diffusion times.

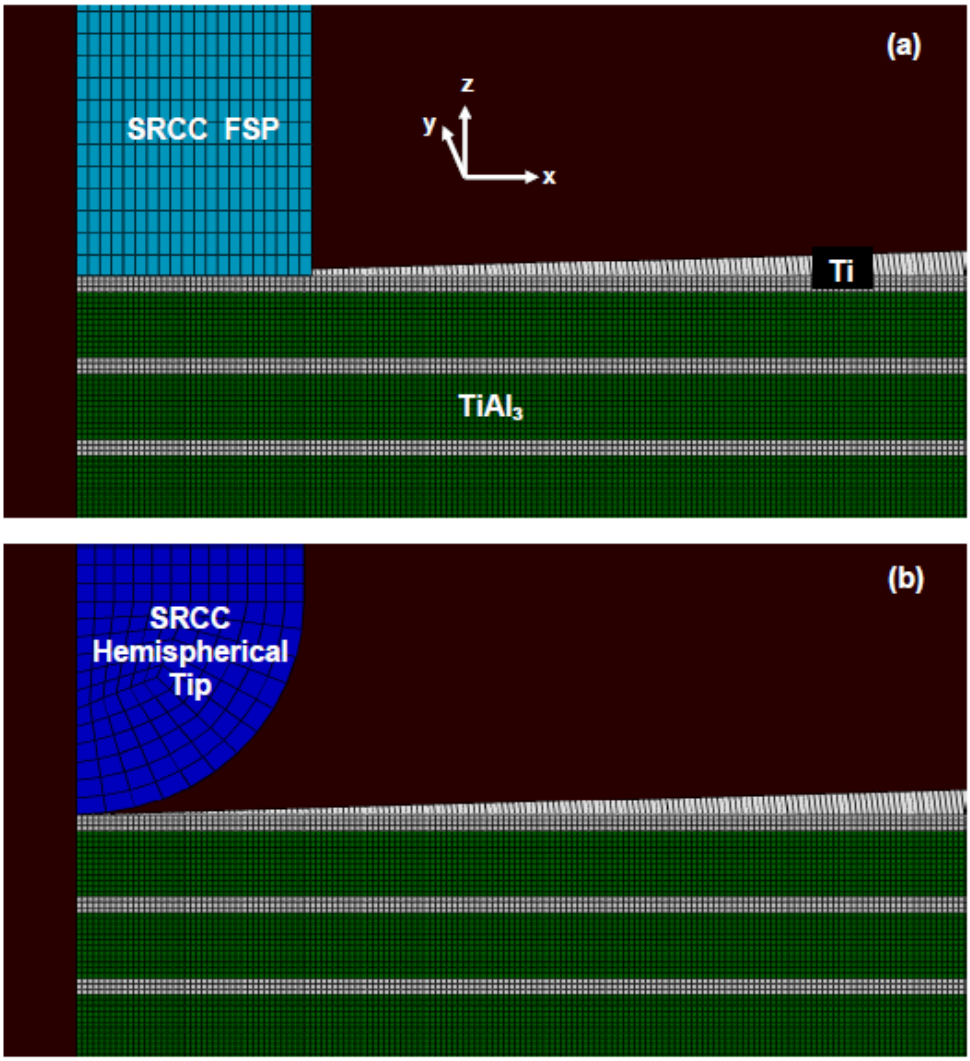

Figure 4. A close-up view of the meshed models, near the rotational axis, of: (a) Tungsten FSP/MILC target-plate; and (b) Tungsten projectile/MILC target-plate.

2.2.4. Initial Conditions

At the start of an analysis, the target-plate is assumed to be stationary while the FSP moves at a normal incident velocity (in the negative z direction) ranging from 500–1500 m/s. In addition, both the FSP and the target-plate are assumed to be stress-free. The use of the latter initial condition for the $Ti/TiAl_3$ MILC target-plate is somewhat problematic since a real target-plate may possess fabrication-induced residual stresses. Although including such residual stresses in the present analysis would be straightforward, no data (experimental or computational) on the spatial distribution of the residual stresses in as-fabricated $Ti/TiAl_3$ MILC target-plates seem to have been published.

2.2.5. Boundary Conditions

Symmetry displacement boundary conditions were applied over radial faces of the 5° sector computational model, i.e. no displacements normal to these faces were allowed. A local rotated coordinate-system was used for the 5° radial face to implement this boundary condition. In addition,

the target-plate bottom-surface nodes having the maximum radial coordinate were prevented from moving in the negative *z*-direction (the rigid back-frame support condition) in order to model the experimental test conditions of Harach [16].

2.2.6. Contact Interactions

Interactions between the FSP and the target-plate and their fragments, as well as self-interactions involving the FSP and the target-plate (and their fragments) are all modeled using the *Hard Contact Pair* type of contact algorithm [19]. Within this algorithm, contact pressures between two bodies are not transmitted unless the nodes on the *slave surface* contact the *master surface*. No penetration/overclosure between the slave and the master surfaces is allowed and there is no limit to the magnitude of the contact pressure that could be transmitted when the surfaces are in contact. Transmission of shear stresses across the contact interfaces is assumed to be controlled by a modified Coulomb friction law. This law uses a static, μ_{st}, and a kinetic, μ_{kin}, friction coefficient and an upper-bound shear stress limit, τ_{slip} (a maximum value of shear stress which can be transmitted before shearing within the softer material, rather than interfacial sliding, begins to take place).

2.2.7. Material Models

Since the material models used are critical and should be described in detail, such a description is deferred to Section 3.

2.2.8. Computational Tool

ABAQUS/Explicit, a general purpose finite-element program [18], was used for all calculations. The problem (formulated in terms of differential equations for mass, momentum and energy conservation along with the material constitutive relations, initial, boundary and contact-interaction conditions) is solved numerically using a finite-element algorithm. A typical transient non-linear dynamics (single 5° sector model) analysis of impact of a FSP onto the $Ti/TiAl_3$ MILC target plate required 12 hours of (wall-clock) time on a 12-core, 3.0 GHz machine with 12 GB of memory. To attain this (reduced) computational cost, variable-mass-scaling and viscous-damping algorithms were employed to help address numerical problems associated with highly distorted finite elements and the resolution of the shock waves generated during an impact event.

3. Material Constitutive Models

Based on the description of the computational domain used, Figures 3(a)-(b), constitutive models for the materials of three sub-components have to be identified: (a) tungsten FSP; (b) Ti laminae; and (c) $TiAl_3$ laminae. In addition, a material model is needed for the $Ti/TiAl_3$ interfaces.

In general, a material (mechanical) model defines relationships between the field/material-state variables (pressure/stress, mass-density/specific volume, energy-density, temperature, etc.). These relationships generally include: (a) an equation of state; (b) a strength model equation(s); and (c) a failure model equation(s). Partitioning of the material model into these three sets of equations follows naturally from representing the total stress tensor as a sum of a hydrostatic stress (scales with negative pressure) tensor (causes a change in the volume of the material) and a deviatoric stress

tensor (causes a change in the shape of the material). The hydrostatic stress is defined by the equation of state which specifies the corresponding functional relationship between pressure, mass-density, and internal-energy density/temperature. The deviatoric stress is defined by the strength model which specifies the functional relations between the deviatoric-stress components and field quantities quantifying the extent and rate of material deformation as well as the effect of material temperature. A failure model defines one or more stress-and/or strain-based conditions, which when attained, cause the material to fracture and lose its ability to support tensile-normal and shear stresses.

In addition, separating the total stress tensor into its hydrostatic and deviatoric parts enables proper modeling of the ability of the materials to support shock and spreading waves. While shock-supporting materials are expected to show nonlinear behavior: (a) normal materials must display an upward curvature in the associated pressure vs. specific volume (reciprocal of the density) plot (i.e., pressure increases at a progressively higher rate as the specific volume decreases); while (b) anomalous materials must display a downward curvature in the associated pressure vs. specific volume plot [20,21,22].

3.1. Tungsten Heavy-Alloy Material Model

The constitutive behavior of Tungsten heavy-alloy is described in terms of: (a) an equation of state; (b) a strength model; and (c) a failure model, in accordance with the preceding discussion.

3.1.1. Equation of State

The shock (i.e. Mie Gruneisen) equation of state is used to represent the hydrostatic part of the material's stress:

$$P(\rho, E) = P^H + \Gamma\rho_0(E - E^H) \tag{1}$$

where P represents pressure, ρ the density, E the mass-based internal energy density, Γ is the *Gruneisen Gamma* parameter, the subscript *o* indicates material reference (usually selected as the initial) state and superscript "*H*" denotes a Hugoniot quantity. The Hugoniot is the (stress vs. specific volume vs. energy density vs. temperature vs. entropy density vs. particle velocity vs. shock speed) locus of the material states generated by the passage of planar stationary shocks of various strengths. For a material, like Tungsten heavy-alloy, for which shock speed U_s varies linearly with particle velocity (i.e. $U_s = C_0 + su_p$, C_0 and s are material specific parameters), density dependence of the Hugoniot pressure is defined as:

$$P^H(\rho) = \frac{\rho_0 C_0^2\left(1 - \frac{\rho_0}{\rho}\right)}{\left[1 - s\left(1 - \frac{\rho_0}{\rho}\right)\right]^2} \tag{2}$$

Since $E^H(\rho)$ is associated with the same Hugoniot as $P^H(\rho)$, $E^H(\rho)$ is not an independent quantity/function and can be related to (or made dependent on) the $P^H(\rho)$ relation through the use of

the *Rankine-Hugoniot* equation [23]. Based on the present description of the shock equation of state, this relation contains three material-specific parameters: C_0, s and Γ_0.

3.1.2. Strength Model

The Johnson-Cook strength model is used to represent the deviatoric part of the material's stress. This model is capable of representing the material behavior displayed under large-strain, high deformation rate, high-temperature conditions, of the type encountered in problems dealing with the interactions of a projectile with target structures. Within the Johnson-Cook model, the elastic part of the deviatoric stress is characterized by a shear modulus which is assumed to be either constant or temperature dependent. The plastic part of the material deviatoric response, on the other hand, is defined by: (i) a von Mises yield criterion which states that the onset and continuation of the plastic deformation requires that the von Mises equivalent stress is larger than the material strength; (ii) a normality flow rule which assumes that the plastic flow of the material takes place in a direction normal to the yield surface; and (iii) a material constitutive relation which defines a plastic strain, strain rate and temperature dependencies of the material's yield strength [24] as:

$$Y = \left[A + B\varepsilon_{pl}^{n}\right]\left[1 + C_1 \log \dot{\varepsilon}_{pl}\right]\left[1 - T_H^{m}\right] \tag{3}$$

where ε_{pl} is the equivalent plastic strain, $\dot{\varepsilon}_{pl}$ the equivalent plastic strain rate, A the zero plastic strain, unit plastic strain rate, room temperature yield strength, B the strain hardening constant, n the strain hardening exponent, C_1 the strain rate constant, m the thermal softening exponent and $T_H = (T - T_{room})/(T_{melt} - T_{room})$ a room temperature (T_{room}) based homologous temperature while T_{melt} is the melting temperature. All temperatures are given in degrees of Kelvin. According to Eq. (3), the plastic deviatoric response of a material is defined by five material-specific parameters A, B, n, C_1 and m, T_{room} and T_{melt}.

3.1.3. Failure Model

The failure behavior of tungsten heavy-alloy was defined using the Johnson-Cook failure model [24], since this material exhibits ductile failure. The progress of failure according to the Johnson-Cook failure model is defined by the following cumulative damage law:

$$D = \sum \frac{\Delta\varepsilon}{\varepsilon_f} \tag{4}$$

where $\Delta\varepsilon$ is the increment in effective plastic strain with an increment in loading and ε_f, is the failure strain at the current state of loading, which is a function of the mean stress, the effective stress, the strain rate and the homologous temperature, given by:

$$\varepsilon_f = \left[D_1 + D_2 \exp(D_3\sigma^*)\right]\left[1 + D_4 \ln \dot{\varepsilon}_{pl}\right]\left[1 + D_5 T_H\right] \tag{5}$$

where σ^* is mean stress normalized by the effective stress. Failure is assumed to occur when $D = 1.0$. According to Eq. (5), ductile failure is controlled by five material-specific parameters D_1, D_2, D_3, D_4 and D_5.

3.1.4. Parameter Identification

The ANSYS/Autodyn material database [25] was the source for the values of the parameters identified in the equation of state, strength and failure material-model. Since only authorized ANSYS/Autodyn users have access to this database, the values of the material-model parameters could not be revealed here.

3.2. Titanium Material Model

Both titanium and tungsten heavy-alloy are metallic materials. For this reason, the constitutive behavior of titanium was also represented using: (a) a shock equation of state; (b) a Johnson-Cook strength model; and (c) a Johnson-Cook failure model. The Titanium material model parameters are also taken from the ANSYS/Autodyn material database but their values could not be released here due to the copyright restrictions.

3.3. $TiAl_3$ Material Model

$TiAl_3$ is an intermetallic compound. However, despite its all-metal content, $TiAl_3$ displays, particularly under high-rate loading conditions, a unique behavior characterized by: (a) a relatively high compressive strength; (b) a substantially lower tensile strength; (c) limited tensile ductility; and (d) low fracture toughness. Consequently, the deformation/fracture behavior of intermetallic compounds like $TiAl_3$ should be represented using a *ceramic-type* material constitutive model. Since the so-called Johnson-Holmquist 2 (JH2) material model [26] is most frequently used to represent the dynamic behavior of intermetallic compounds, this type of model is adopted, in the present work, to describe the behavior of $TiAl_3$.

Within the JH2 material model, two terminal material states: (a) an intact material; and (b) a failed material, are postulated. The two material states are weighted by a single scalar variable called damage, D, whose evolution is governed by an inelastic (plastic-like) deformation model. The JH2 model also comprises: (a) an equation of state; (b) a strength model; and (c) a failure model.

3.3.1. Equation of State

The JH2 material model describes the hydrostatic response of a material by a polynomial equation of state in which the pressure is assumed to be independent of the internal-energy density. The pressure vs. degree-of-compression relation in a damage-free material is defined as:

$$P = K_1\mu + K_2\mu^2 + K_3\mu^3, \quad \mu > 0 \quad (hydrostatic\ \ compression) \tag{6}$$

and

$$P = K_1\mu, \quad \mu < 0 \quad (hydrostatic\ \ tension) \tag{7}$$

where degree-of-compression is $\mu = (\rho/\rho_0 - 1)$ and ρ is the current density, while ρ_0 (the reference density), K_1 (the bulk modulus), K_2 and K_3 are material-specific constants.

Once the subject material is damaged (i.e. when the extent of damage is finite, $D > 0$), Eq. (7) must be upgraded to include the effect of bulking. Bulking is a phenomenon associated with the fact that fragments of fractured materials are not generally fully conformable, and consequently, fractured material is associated with a larger volume (a lower density at a constant pressure) than the damage-free material. The bulking-modified polynomial equation of state is then given by:

$$P = K_1\mu + K_2\mu^2 + K_3\mu^3 + \Delta P, \quad \mu > 0 \tag{8}$$

where the bulking-induced pressure increment, ΔP, is determined from energy considerations and varies from zero at $D = 0$ to ΔP_{max} at $D = 1.0$. Assuming that a fraction of the internal elastic energy decrease (due to decrease in deviatoric stresses in the material) is converted to an increase in potential internal energy, the bulking-induced pressure increment ΔP at a time $t+\Delta t$ can be represented in terms of ΔP at the time t as:

$$\Delta P(t+\Delta t) = -K_1\mu(t+\Delta t) + \sqrt{(K_1\mu(t+\Delta t) + \Delta P(t))^2 + 2\beta K_1 \Delta U} \tag{9}$$

where ΔU is the decrease in deviatoric elastic energy due to damage-induced yield-strength reduction and β is the fraction of the deviatoric elastic energy converted to hydrostatic potential/elastic energy. The decrease in deviatoric elastic energy is given by:

$$\Delta U = U_t - U_{t+\Delta t} \tag{10}$$

where

$$U_t = \frac{\sigma_t^2}{6G} \tag{11}$$

In Eq. (11), σ_t represents the actual compressive yield strength at time t while G, a material parameter, denotes the damage-free shear modulus of the subject material. Eqs. (6)–(11) show that the JH2 parameters: K_1, K_2, K_3, β, and G define the hydrostatic response of the subject material.

3.3.2. Strength Model

The JH2 strength model combines the von Mises yield criterion and normality flow rule with a pressure and strain-rate hardening constitutive relation. The latter is described using a normalized yield strength defined as a damage-weighted rule of mixtures of the corresponding damage-free and fractured yield strengths as:

$$\sigma^* = \sigma_i^* - D(\sigma_i^* - \sigma_d^*) \tag{12}$$

where subscripts i and d are used to denote intact and damaged material states and the superscript * indicates that the corresponding yield strength is normalized by the Hugoniot Elastic Limit (HEL) (uniaxial strain) yield strength, i.e.:

$$\sigma^* = \frac{\sigma}{\sigma_{HEL}} \tag{13}$$

The normalized yield strengths σ_i^* and σ_d^* are also defined in the same manner as σ^*. The normalized (pressure- and strain-rate-dependent, ideal-plastic) yield strength of the damage-free material, σ_i^*, and the fractured material, σ_d^*, are respectively given by:

$$\sigma_i^* = A(P^* + T^*)^N (1 + C \ln \dot{\varepsilon}^*) \tag{14}$$

$$\sigma_d^* = B(P^*)^M (1 + C \ln \dot{\varepsilon}^*) \tag{15}$$

where A, B, C, M, N and σ_{HEL} appearing in Eqs. (13)–(15) are all material-specific parameters while P^* and T^* are respectively defined as:

$$P^* = \frac{P}{P_{HEL}} \tag{16}$$

and

$$T^* = \frac{T}{P_{HEL}} \tag{17}$$

where P and T are the actual pressure and the maximum hydrostatic tensile pressure that the subject material can withstand, respectively, and P_{HEL} is the pressure at the Hugoniot Elastic Limit. Finally, the dimensionless material strain rate, $\dot{\varepsilon}^*$, appearing in Eqs. (14) and (15) is defined as:

$$\dot{\varepsilon}^* = \frac{\dot{\varepsilon}}{\dot{\varepsilon}_0} \tag{18}$$

where $\dot{\varepsilon}$ is the actual strain rate and $\dot{\varepsilon}_0$ is the reference strain rate (set in the present work to 1.0 s^{-1}).

Eqs. (12)–(18) show that the JH2 parameters: A, σ_{HEL}, P_{HEL}, B, C, M, and N define the deviatoric response of the subject material.

3.3.3. Failure Model

The JH2 failure model defines the evolution/accumulation of damage as:

$$D = \sum \frac{\Delta \varepsilon_p}{\varepsilon_p^f} \tag{19}$$

where $\Delta\varepsilon_p$ is the increment in equivalent inelastic strain with an increment in loading and the failure strain ε_p^f is a pressure-dependent equivalent fracture strain which is defined as:

$$\varepsilon_p^f = D_{1,JH2}(P^* + T^*)^{D_{2,JH2}} \tag{20}$$

where $D_{1,JH2}$ and $D_{2,JH2}$ are material specific parameters.

This model defines two fracture criteria: either (i) damage reaches a critical value of 1.0; or (ii) negative pressure reaches a value of *T*. Fractured material has no ability to support any negative pressure, while its ability to support shear is defined by Eq. (15). Eqs. (13)–(20) show that the JH2 failure model parameters: $D_{1,JH2}$ and $D_{2,JH2}$ define the failure response of the subject material.

3.3.4. Parameter Identification

Since the values of the equation of state, strength and failure material-model parameters identified above are all taken from Ref. [27], they will not be repeated here.

3.4. Ti/TiAl$_3$ – Interface Material Model

It is well-established experimentally [10] that bonding between Ti and $TiAl_3$ lamellae is relatively weak. The extent and the nature of damage sustained by the Ti/$TiAl_3$ MILC target plate when impacted by a high-velocity FSP can be substantially affected by this weak bonding. These findings indicate that, a high fidelity material model is required for the Ti/$TiAl_3$ inter-lamellar boundaries for accurate modeling of the Ti/$TiAl_3$ MILC target plate impact/penetration behavior.

3.4.1. Cohesive Zone Interface-Model Formulation

The cohesive zone framework originally introduced by Needleman [28] is employed to model the Ti/$TiAl_3$ interfaces. The cohesive zone is assumed to have a negligible thickness when compared with other characteristic lengths of the problem, such as the interfacial in-plane dimensions, characteristic lengths of the mechanical-quantity fields, etc. The mechanical behavior of the cohesive zone is characterized by a traction (i.e. force per unit interface area, in the deformed configuration) vs. interfacial displacement-jump relation, which is introduced through the definition of an interface potential, Ψ. Stable equilibrium of the interface (the initial, stress-free state) corresponds to the case of complete bonding, where the potential has a minimum and all tractions vanish. For any other configuration, the value of the potential is taken to depend only on the interfacial displacement jump. In the present work, the tangential/sliding behavior of the interface is assumed to be isotropic, so that the cohesive-zone model can be formulated within a two-dimensional framework. In this case, the interface displacement jump is expressed in terms of its normal component, U_n, and a tangential component, U_t.

The normal and tangential components of the traction vector F are obtained by differentiating the interface potential function $\Psi = \hat{\Psi}(U_n, U_t)$ with respect to U_n and U_t, respectively,:

$$F_n(U_n, U_t) = \frac{-\partial \hat{\Psi}(U_n, U_t)}{\partial U_n} \tag{21}$$

$$F_t(U_n, U_t) = \frac{-\partial \hat{\Psi}(U_n, U_t)}{\partial U_t} \tag{22}$$

The interface constitutive relations are fully defined by specifying the form for the interface potential function $\hat{\Psi}(U_n, U_t)$. The interface potential of the following form initially proposed by Socrate [29], is used in the present study

$$\hat{\Psi}(U_n, U_t) = \left(-e\sigma_{\max}\delta_n + \frac{1}{2}\tau_{\max}\delta_t \log\left[\cosh\left(2\frac{U_t}{\delta_t} \right) \right] \right) \left[\left(1 + \frac{U_n}{\delta_n} \right) \exp\left(-\frac{U_n}{\delta_n} \right) \right] \tag{23}$$

where the parameters $\sigma_{\max}$ and $\tau_{\max}$ are, respectively, the normal and tangential interfacial strengths, and δ_n and δ_t are the corresponding characteristic interface lengths. Differentiation of Eq. (23) with respect to U_n and U_t yields the expressions for the interfacial tractions

$$F_n(U_n, U_t) = \left(e\sigma_{\max} - \frac{1}{2}\tau_{\max}\frac{\delta_t}{\delta_n} \log\left[\cosh\left(2\frac{U_t}{\delta_t} \right) \right] \right) \left[\frac{U_n}{\delta_n} \exp\left(-\frac{U_n}{\delta_n} \right) \right] \tag{24}$$

$$F_t(U_n, U_t) = \left[\tau_{\max} \tanh\left(2\frac{U_t}{\delta_t} \right) \right] \left[\left(1 + \frac{U_n}{\delta_t} \right) \exp\left(-\frac{U_n}{\delta_n} \right) \right] \tag{25}$$

Graphical representation of the two functions defined by Eqs. (24) and (25) is given in Figures 5(a)-(b). It should be noted that, for convenience, the quantities plotted along the *x*, *y* and *z* axes are properly normalized. If F_n given by Eq. (24) is expressed for the case of purely normal interface decohesion, and F_t for the case of pure sliding, one obtains:

$$F_n(U_n, U_t = 0) = F_n^0(U_n) = e\sigma_{\max} \left[\frac{U_n}{\delta_n} \exp\left(-\frac{U_n}{\delta_n} \right) \right] \tag{26}$$

$$F_t(U_n = 0, U_t) = F_t^0(U_t) = \tau_{\max} \tanh\left(2\frac{U_t}{\delta_t} \right) \tag{27}$$

Eqs. (26) and (27) indicate that the interface behavior is characterized by four parameters: $\sigma_{\max}$, δ_n, $\tau_{\max}$ and δ_t, where $\sigma_{\max}$ is the peak normal traction for purely normal interface decohesion, δ_n is the normal interface separation, which corresponds to this peak traction, $\tau_{\max}$ is an asymptotic shear traction for interface sliding, and δ_t is a characteristic length in pure sliding, which corresponds to a shear traction within 1% $\tau_{\max}$ ($F_t^0(\delta_t) \approx 0.99\tau_{\max}$). These four parameters are determined, in the present work, as a function of the relative crystallographic orientation of the Ti and $TiAl_3$ phases and as a function of the orientation of the Ti/$TiAl_3$ interface using a combination of the virtual mechanical testing procedure and the molecular-statics analysis (as described in the next subsection).

3.4.2. Parameterization of the Interface Model Using Atomic-scale Virtual Mechanical Testing

A number of Ti/$TiAl_3$ interfaces were modeled in this study, each characterized by the specific relative crystallographic orientation of the two phases and by the orientation of the (planar) interface. For each such case, an atomistic h.c.p-Ti/$TiAl_3$ bicrystal was first constructed. An example of such a bicrystal is given in Figure 6(a). For clarity, Ti and Al atoms are assigned different colors and labeled. Figure 6(a) corresponds to the case of the following relative crystallographic orientation between the two phases: (a) $(0\ 0\ 0\ 1)_{Ti} \parallel (1\ 1\ 2)_{TiAl3}$, i.e. the close-packed planes of the two phases are parallel; and (b) $[1\ 1\ -2\ 0]_{Ti} \parallel [1\ -1\ 0]_{TiAl3}$, i.e. the close-packed directions are parallel. Furthermore, the Ti/$TiAl_3$ interface in Figure 6(a) is parallel to the previously identified close-packed planes of the two phases. To help parameterize the cohesive-zone interface model, described in the previous section, bicrystals like the one shown in Figure 6(a) are subjected to a virtual mechanical testing procedure (described below). Such a procedure is carried out within an atomistic/molecular environment, within which the subject material(s) is modeled as an assembly of the interacting atoms. In the present work, Ti-Ti, Ti-Al and Al-Al atomic two-atom, as well as multi-atom, interactions are described using the so-called embedded atom method (EAM) forcefields [30,31]. Within the EAM framework, the potential energy E_t of a system containing N atoms can be written as

$$E_t = \sum_{i}^{N} F_i^I\left(\sum_{j\neq i}^{M} f_i^I\left(r_{ij}\right)\right) + \frac{1}{2}\sum_{\substack{i,j \\ (i\neq j)}}^{M} \varphi_{ij}^{IJ}\left(r_{ij}\right) \tag{28}$$

where F_i^I is the energy required to embed atom i of species $I = \alpha$, β into the electron density $\sum_{j\neq i}^{M} f_i^I\left(r_{ij}\right)$ associated with the M neighbors of atom i within a cut-off radius; $f_i^I\left(r_{ij}\right)$ is the spherically averaged (atomic) electron density at the location of atom i due to atom j at the inter-atomic distance r_{ij}. $\varphi_{ij}^{IJ}\left(r_{ij}\right)$ is the core-core pair interaction potential between atom i of species $I = \alpha$, β and atom j of species $J = \alpha$, β separated by the distance r_{ij}. In the present case, α = Al and β = Ti. The functional

forms for the embedding energy, electron density and core-core pair interaction potential for the Ti/TiAl3 system are shown in Figures 7(a)-(c), respectively.

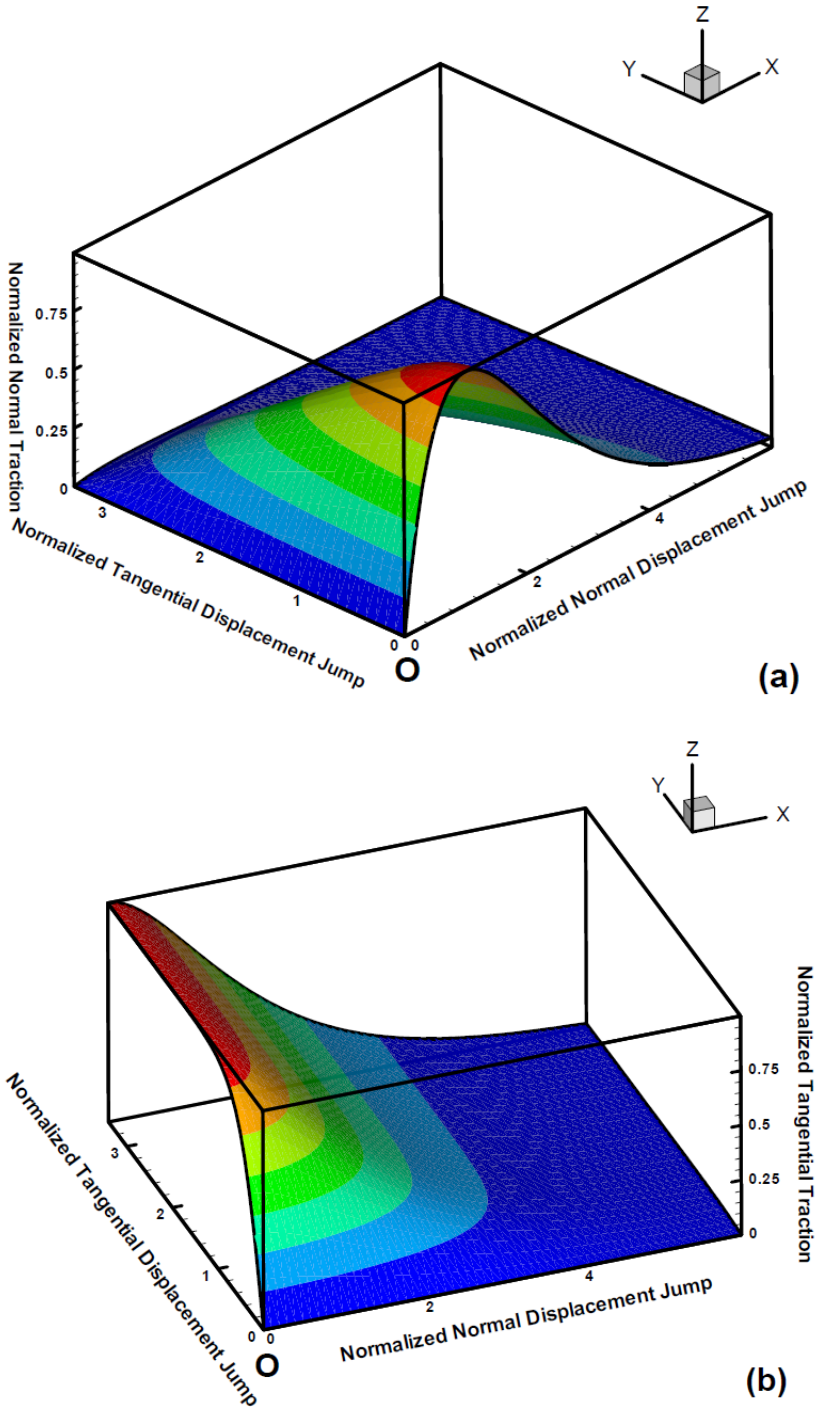

Figure 5. Normalized: (a) normal, F_n; and (b) tangential, F_t, components of the traction per unit interface area, as a function of the normalized (normal, U_n, and tangential, U_t) components of the interface displacement jumps. The coordinate system origin is denoted by "O."

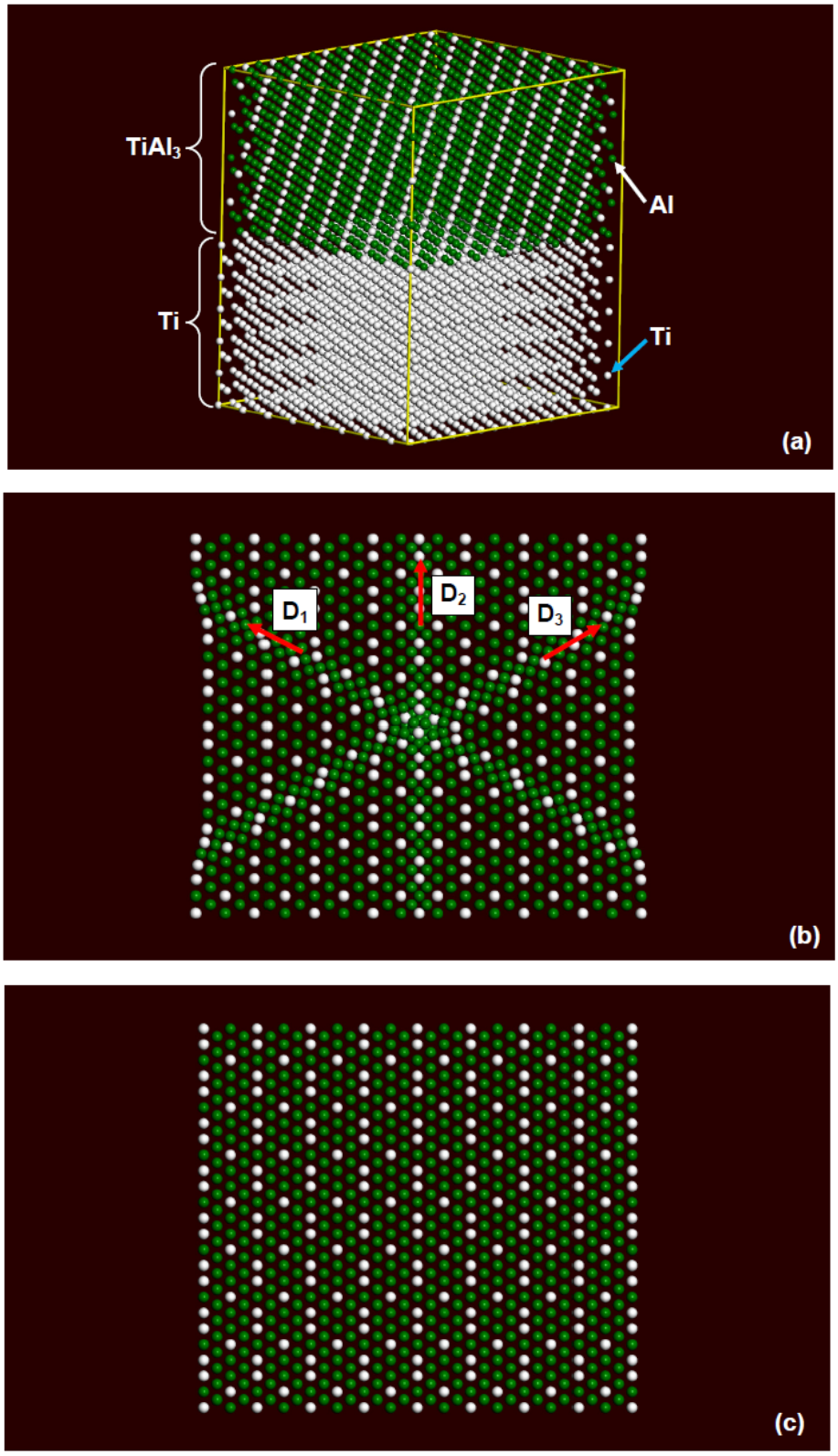

Figure 6. (a) Example of atomic-scale computational bicrystal used to determine the $Ti/TiAl_3$ interface decohesion potential, through virtual mechanical tests; (b) three $(1\ 1\ 2)_{TiAl3}$ close-packed planes adjacent to the $Ti/TiAl_3$ interface, with three anti-coherency interfacial dislocations denoted by D_1-D_3; and (c) the same three $(1\ 1\ 2)_{TiAl3}$ close-packed planes in the perfect $TiAl_3$ structure.

The EAM forcefield parameterization used correctly predicts the room-temperature, stable crystal structures: (a) h.c.p for Ti; and (b) $D0_{22}$ (an ordered body-centered tetragonal structure).

The virtual mechanical testing procedure involved the following steps:

(a) Before constructing the computational bicrystals, the EAM method is validated by reproducing, with sufficient accuracy, the 0 K lattice parameters of the two phases (a_{Ti} = 0.295 nm; a_{TiAl3} = 0.384 nm, c_{TiAl3} = 0.858 nm). This was accomplished through the use of a conjugate-gradient method-based potential-energy minimization (i.e. molecular statics) procedure;

(b) The 0 K equilibrium structure of the $Ti/TiAl_3$ interface in each case is determined by employing the aforementioned molecular-statics procedure under flexible periodic boundary conditions in two directions parallel to the interface and the free surface boundary conditions in the direction normal to the interface. The use of the free surface boundary conditions allows the spacing of the planes parallel to and near the interface to adjust to the differences in the atomic environment. The equilibrium atomistic configuration for the ($TiAl_3$-side of the) $Ti/TiAl_3$ interface corresponding to the bicrystal given in Figure 6(a), is shown in Figure 6(b). For comparison, the corresponding perfect $TiAl_3$ atomistic configuration is displayed in Figure 6(c). Comparison of the atomistic configurations displayed in Figures 6(b)-(c) reveals the presence of three families of the so-called "anti-coherency" interfacial dislocations (labeled D_1–D_3), i.e. line-type of defects which account for the presence/absence of the extra half planes across the interface [32,33]. Interfacial regions separated by these dislocations are associated with the "forced" crystallographic-plane continuity across the interface and can be also represented in terms of the so-called "coherency" interfacial dislocations [32,33]; and

(c) In the case of each bicrystal, the two adjoining crystals are displaced, relative to each other, by the prescribed amounts (U_n and U_t) in the normal and tangential directions, respectively. The potential energy of each bicrystal is next minimized under the constraint that the average displacements of the atoms within the two (one Ti and one $TiAl_3$) interfacial planes remain equal to the prescribed interfacial displacement $U = [U_n, U_t]$. The difference between the energies of the bicrystal in the displaced configuration and in the initial equilibrium configuration expressed per unit area of the interface is then defined as the value of the interface decohesion potential, Ψ, at the given values of U_n and U_t. This procedure is repeated over a range of values for the two interfacial displacements, and the results obtained are used in conjunction with a nonlinear multiple regression analysis to determine the values of the four aforementioned interfacial-model parameters. It should be noted that, due to the periodic nature of the interface structure, the employed virtual mechanical testing procedure predicts a periodic interface potential relative to the tangential displacements. To comply with the form of the interface potential given by Eq. (23), only the portion of the atomistic simulation results that show an increase of F_t with U_t is used and fitted using the functional relationships defined by Eq. (23). The procedure employed yielded a specific set of four interfacial-model parameters for each of the bicrystals analyzed. In the absence of the experimental results revealing the preferred nature of the relative orientation relationship between the Ti and $TiAl_3$ phases and the $Ti/TiAl_3$ -interface orientation, a unique set of the four parameters is obtained using a simple averaging scheme. This procedure yielded the following mean values and the corresponding one

standard-deviation ranges: σ_{max} = 7.29 ± 0.36 GPa, δ_n = 0.09 ± 0.005 nm, τ_{max} = 1.20 ± 0.06 GPa and δ_t = 0.33 ± 0.02 nm. Only the mean values of the four parameters are used in the finite-element analysis of the Ti/$TiAl_3$ MILC impact behavior.

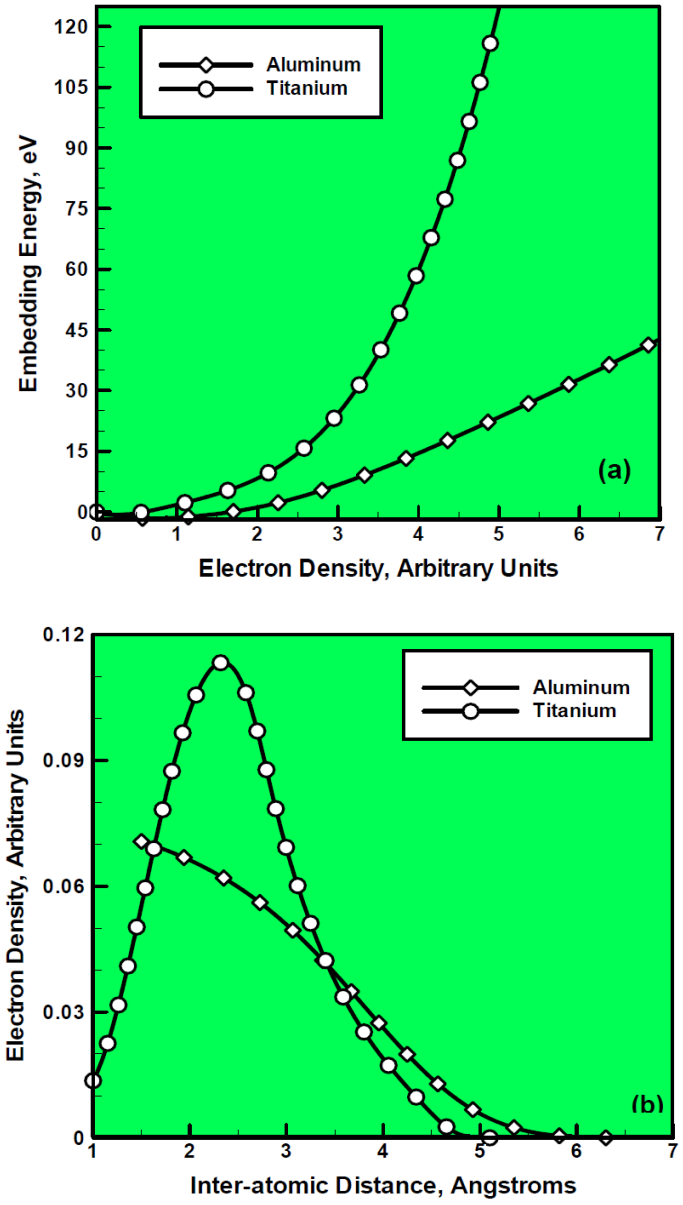

Figure 7. EAM functional relationships for the binary Ti-Al system used in the present work: (a) Embedding energy vs. electron density; (b) electron density vs. inter-atomic spacing; and (c) core-core pair interaction energy vs. inter-atomic spacing.

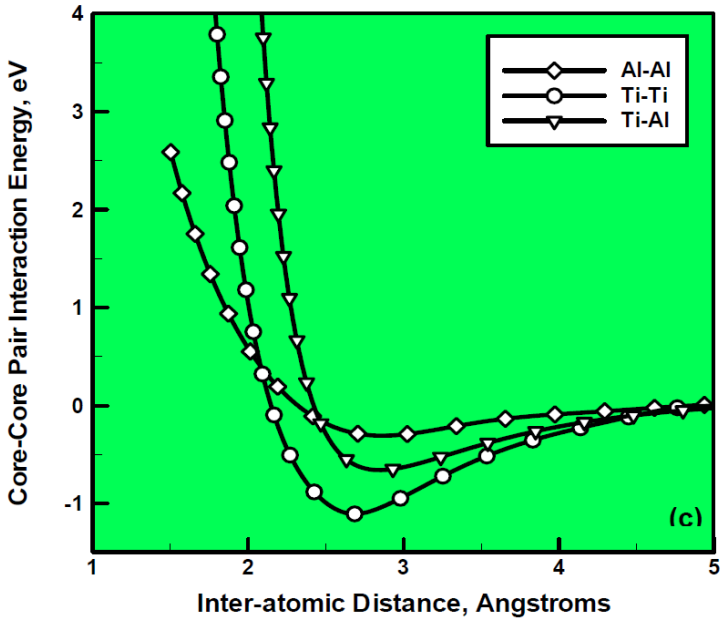

Figure 7. Continued.

4. Results and Discussion

First, the proposed multi-scale computational approach is validated by comparing the computational results obtained for the case of 900 m/s normal impact by the SRCC projectile with a hemispherical tip with experimental data. Then, the efficiency of ballistic protection offered by the $Ti/TiAl_3$ MILC protective structures is assessed using the computed results for the cases of the normal impact by SRCC FSP at different incident velocities.

4.1. Multi-scale Computational Model Validation

Apparently the sole publicly available source of experimental data for the ballistic-impact behavior and performance of $Ti/TiAl_3$ MILC target plates is Harach [16]. These experimental results were obtained under the following test conditions: (i) 900 m/s normal impact by a 10-g/6.15-mm diameter, heavy tungsten alloy SRCC projectile with a hemispherical tip; onto (ii) a 20-mm thick $Ti/TiAl_3$ MILC composite plate containing approximately 20 vol. % of Ti (mass density = 3.5 g/cm^3; areal density = 7 g/cm^2). Two types of results were reported: (a) the total depth of penetration (approximately 10 mm); and (b) a macrograph of the target-plate normal-transverse cross-section passing through the center of the cylindrical hole made by the impactor. Examination of this macrograph, depicted schematically in Figure 8(a) reveals that:

(i) the $Ti/TiAl_3$ MILC target plate has a complex deformation/damage/failure response to impact by the projectile;

(ii) the Ti phase, which possesses a high level of ductility, deforms substantially and ultimately fails in either the strain-localization or shear-fracture mode;

(iii) the $TiAl_3$ phase displays brittle behavior and tends to fracture quite readily and to produce numerous cracks and fragments. This finding is fully consistent with the previously-established mechanical properties of this phase; i.e. while the compressive strength and stiffness of this phase are

quite high, the ambient-temperature fracture toughness (K_{1C} = 2 MPa $m^{1/2}$) is quite low. This lack of fracture toughness in $TiAl_3$ can be attributed to the limited mobility of unit dislocations (as well as paired superdislocations separated by anti-phase boundaries), insufficient number of slip or twinning systems, and/or very low surface energy which promotes brittle fracture over dislocation emission at the crack tip;

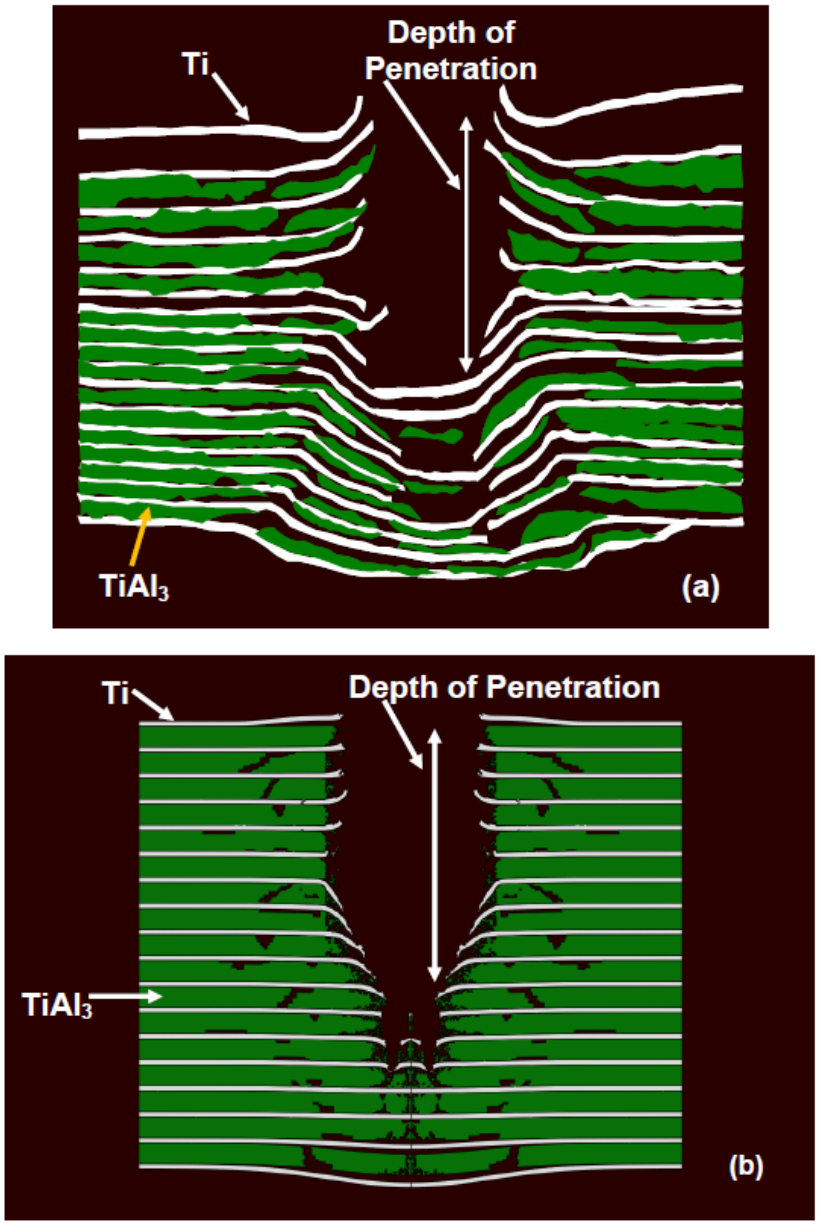

Figure 8. Post-mortem analysis of the deformation and damage sustained by a Ti/$TiAl_3$ MILC target plate (having a thickness of 20 mm and containing 20 vol.% Ti), after normal impact by a SRCC heavy tungsten alloy (10-gram, 6.15 mm diameter) projectile with a hemispherical cap, initially propelled at 900 m/s: (a) schematic of experimental macrograph showing the target-plate normal-transverse cross-section passing through the center of the cylindrical hole made by the impactor [16]; and (b) corresponding computational results.

(iv) the MILC is highly susceptible to delamination due to the low adhesion strength of $Ti/TiAl_3$ interfaces. It should be noted that in Figure 8(a), which is a schematic of an optical macrograph depicted in Ref. [16], many originally present loose fragments of $TiAl_3$ are not seen since they have been "lost" during the process of target-plate sectioning. This fact should be taken into account when comparing the experimental results shown in this figure with their computational counterparts presented and discussed later in this subsection (since similar loss of the loose fragments does not take place within the computational framework employed); and

(v) a major portion of the material is missing from the back-face of the impacted MILC target plate. One can expect that the missing material was propelled away from the back-face of the target plate in the form of high-velocity spall fragments during the ballistic impact.

Figure 8(b) shows the computational results corresponding to the experimental ones shown in Figure 8(a). When the results displayed in Figures 8(a)-(b) are compared, the following can be established: (a) the computed depth of penetration by the projectile, Figure 8(b), is in reasonable agreement with its experimental counterpart, Figure 8(a); and (b) the nature and the spatial distribution of the deformation, damage and failure mechanisms predicted by the present computational analysis, Figure 8(b), are comparable with their experimental counterparts, Figure 8(a).

These results and observations indicate that the present multi-scale computational approach can be expected to yield realistic predictions of the overall ballistic-protection efficiency of the $Ti/TiAl_3$ MILC protective structures.

4.2. Analysis of the Stress Wave Generation, Propagation and Interaction

Since a $Ti/TiAl_3$ MILC target plate is made of a laminated composite material, its ballistic response is expected to be highly affected (if not dominated) by the details of stress wave generation, propagation and interaction within the target plate during impact. To help understand the effect of stress-wave physics on the ballistic response of laminated-composite target plates, a brief analysis of the stress-wave physics within a laminated structure is presented in this subsection. In such an analysis, one of the key parameters is the so-called acoustic impedance, $I_a = C\rho = \sqrt{E\rho}$, where C is the sound speed, ρ is the mass density and E is the Young's modulus.

Impact of a laminated-composite target plate by a projectile is associated with the following sequence of stress-wave phenomena and processes:

(a) As a result of the initial impact of the projectile/FSP onto the target, a compressive (normal) stress wave is produced within the first lamella (Ti in the present case), and travels toward the back face of the target plate;

(b) The arrival of this wave at the first $Ti/TiAl_3$ interface generates a transmitted, compressive wave (also traveling toward the back-face of the target plate), within the first $TiAl_3$ lamella;

(c) To determine the compressive/tensile character of the reflected wave, propagating within the first $TiAl_3$ lamella towards the front face of the target, one must know the acoustic impedances of the two ($Ti/TiAl_3$) contacting materials. Based on the values of E and ρ for Ti and $TiAl_3$, their acoustic impedances are found to be ~22.9 and ~27.0 MPa kg/m^3. Based on the elementary stress-wave/material-interface analysis, and the recognition that $TiAl_3$ is an acoustically stronger material than Ti, the reflected wave, in this case, is of a compressive character;

(d) The same analysis reveals that when the transmitted compressive stress wave reaches the first $TiAl_3$/Ti interface, a transmitted compressive stress wave is produced in the second Ti lamella and a reflected tensile wave in the first $TiAl_3$ lamella;

(e) The interaction of the last transmitted stress wave with the Ti/$TiAl_3$ interface is qualitatively identical to that identified for the incident compressive wave, points (b) and (c);

(f) In the same manner fashion, the findings presented in (b)-(d) can be used to infer the outcome of the interactions of the subsequent transmitted waves with the subsequent interfaces;

(g) When the transmitted compressive wave ultimately encounters the last Ti lamella, with the backface free surface, a reflected tensile/release stress wave forms and travels towards the front face of the target. When this stress wave reaches the last Ti/$TiAl_3$ interface, a transmitted tensile wave is produced within the last Ti lamella (as well as in the subsequent $TiAl_3$ lamella). The presence of these tensile stress waves (originating at the target backface and propagating towards the target frontface) within the brittle $TiAl_3$ phase is expected to promote its cracking/fragmentation. In addition, the arrival of these waves to the Ti/$TiAl_3$ boundaries is expected to promote delamination and spalling;

(h) The reflected tensile wave within the top-most $TiAl_3$ lamella will also cause promote $TiAl_3$ fracture/fragmentation and delamination (as well as the reflected tensile waves generated in the subsequent $TiAl_3$ lamellae). Fracture/fragmentation of the brittle $TiAl_3$ can also result from the compressive stresses found in the vicinity of the advancing projectile/FSP; and

(i) One of the most important outcomes of the analysis presented above is that, despite the fact that the advancing projectile/FSP imparts compressive stress waves into the target structure, a significant part of the target-plate volume ahead of, and surrounding, the projectile/FSP will experience tensile stresses because the stress-waves propagation velocity is several times higher than that of the projectile and in the laminated composite, there is a large number of inter-material boundaries at which complex wave transmission and reflection processes take place. This point is supported by the (100 m/s incident velocity) FSP-impact results displayed in Figure 9, which clearly shows predominance of the tensile stresses within the target plate when the FSP has penetrated the topmost Ti layer and approximately one-third of the topmost $TiAl_3$ layer.

It should be noted that, in order to produce the through-the-thickness normal stress field results presented in Figure 9, the interfacial cohesive elements were not allowed to fail/delaminate through the use of artificial strengthening. When delamination was allowed, the stress fields were still dominated by their tensile component, but the character of the fields were much more complex.

It should be also noted that within the stress-wave physics analysis presented above, the interaction among various (multiply) reflected and transmitted waves was not included. Such interactions can locally produce amplified stress levels causing highly localized damage/failure. Also excluded from the analysis are the roles of the Poisson's effect and the lateral constraints within the target plate, which can produce shear stresses, which in turn can play an important role in the fracture of the ductile Ti phase.

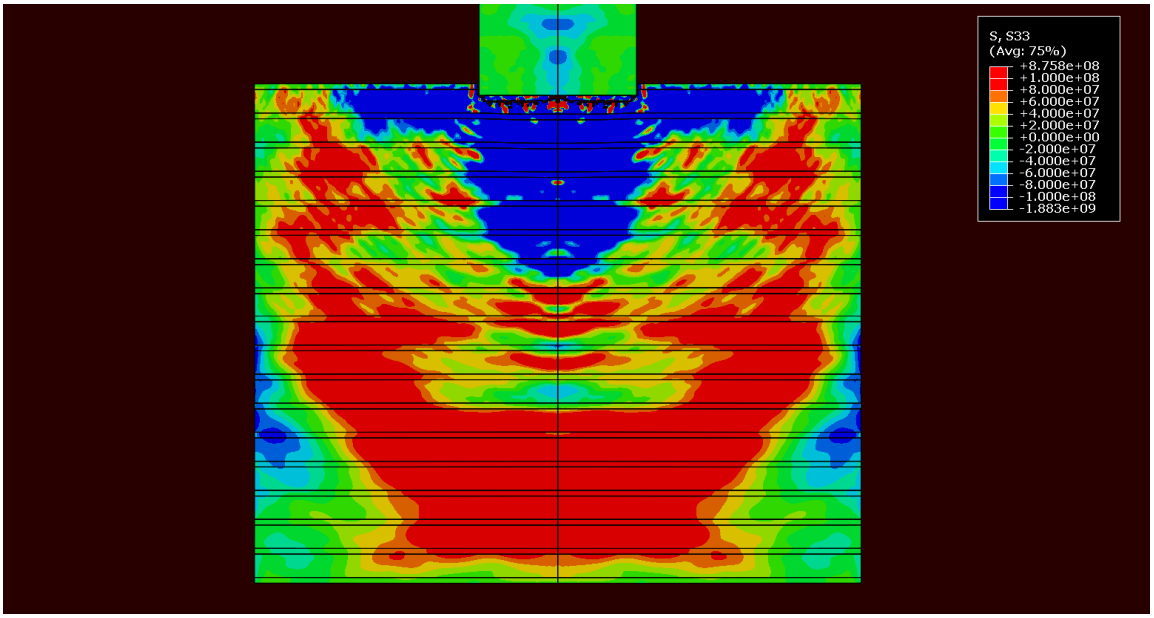

Figure 9. Distribution of the normal stress through the thickness of the target plate when the FSP, initially propelled at 100 m/s, has penetrated the topmost Ti layer and approximately one-third of the topmost $TiAl_3$ layer. Tensile stresses are seen to be predominant.

4.3. Material Evolution During FSP/Target-Plate Impact

Figures 10(a)-(d) show temporal evolution and spatial distribution of the FSP and the Ti/$TiAl_3$ MILC target-plate materials during the 900 m/s normal (i.e. zero-obliquity angle) impact by the FSP. This value of the FSP velocity is one of the lowest values which ensures a complete penetration of the target plate. It should be noted that in order to help reveal the deformation and damage sustained by the FSP and target plate, 36 adjacent 5° sectors (= 180°) for the FSP and the target plate are depicted in Figures 10(a)-(d). Examination of the results displayed in Figures 10(a)-(d), as well as of the similar results (not shown for brevity) obtained in the present work, revealed:

(a) Plastic deformation takes place exclusively within the ductile Ti phase while damage and fracture is localized within the brittle $TiAl_3$ phase in the region ahead of (and surrounding) the FSP, in the early stages of the FSP/target plate interaction;

(b) The extent of plastic deformation within Ti increases and this phase begins to fail by a combination of excessive stretching and shearing as the FSP continues to penetrate the target plate. Simultaneously, $TiAl_3$ acquires increasingly more damage and the damage spreads both in the direction of FSP motion and laterally. Furthermore, delamination at the Ti/$TiAl_3$ interfaces commences and starts to play a significant role in the impact-response of the target plate;

(c) In many instances, delamination is the result of deflection of the $TiAl_3$-borne cracks arriving at, and expanding parallel to, the $TiAl_3$/Ti interface. In other words, cracks generated within the neighboring $TiAl_3$ lamellae do not readily enter the Ti layer and in turn, the next $TiAl_3$ layer. Thus, Ti lamellae act as a crack-bridging medium delaying the formation of large through-the-thickness crack within the MILC target-plate. Only after the opening displacements of the cracks residing in the neighboring $TiAl_3$ lamellae have reached relatively large values and subjected the Ti crack bridge

to large tensile/shear stresses (causing the bridge to fail), can the larger cracks spanning multiple lamellae form;

(d) The last stage of the FSP/target plate interaction is characterized by continued fragmentation of the $TiAl_3$ phase, as well as of the Ti phase, together with pronounced activity of delamination and spall-fragment formation;

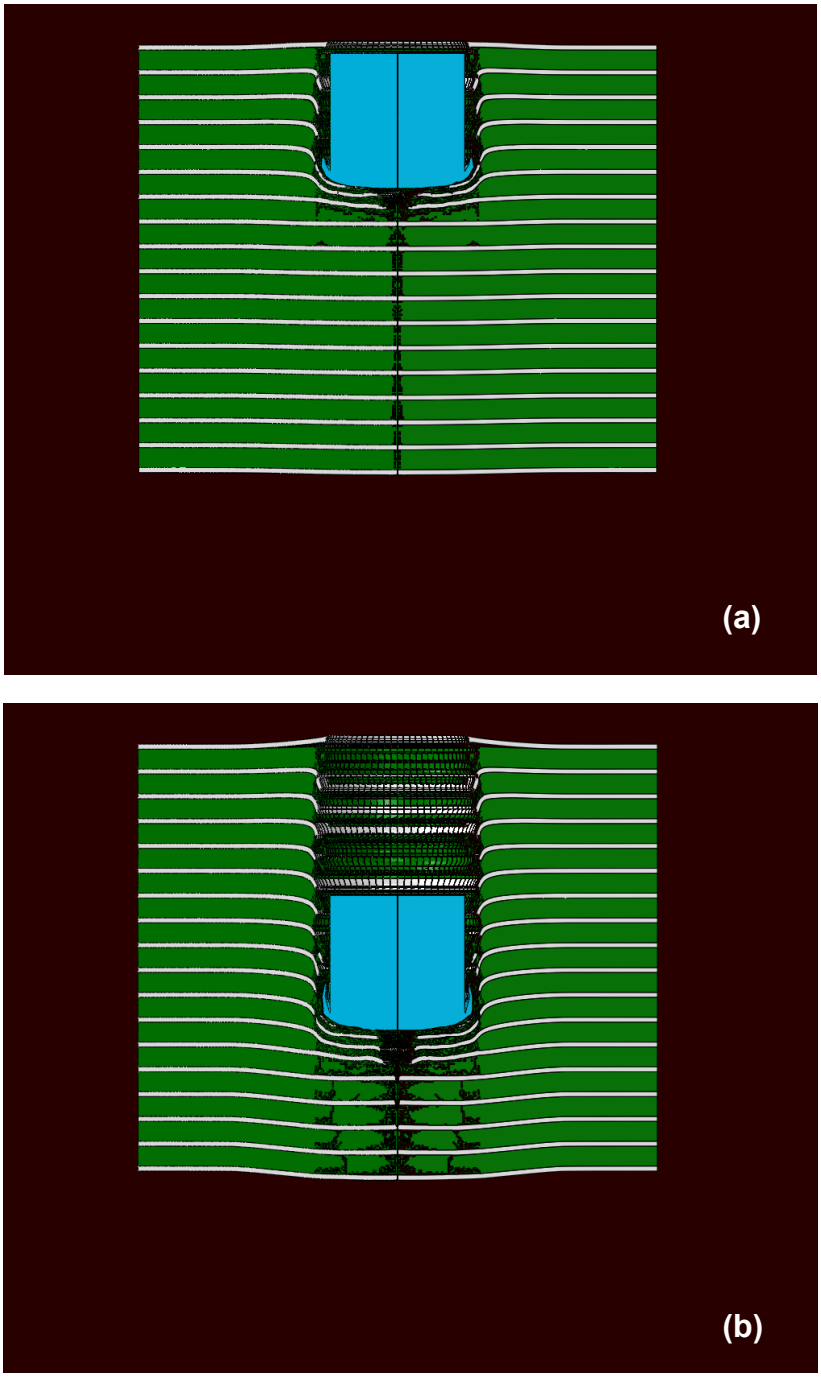

Figure 10. Evolution and distribution of the materials of the FSP and the Ti/$TiAl_3$ MILC target-plate during the 900 m/s normal impact by the FSP, at post-impact simulation times of: (a) 7.65 μs; (b) 15.21 μs; (c) 22.65 μs; and (d) 30.00 μs.

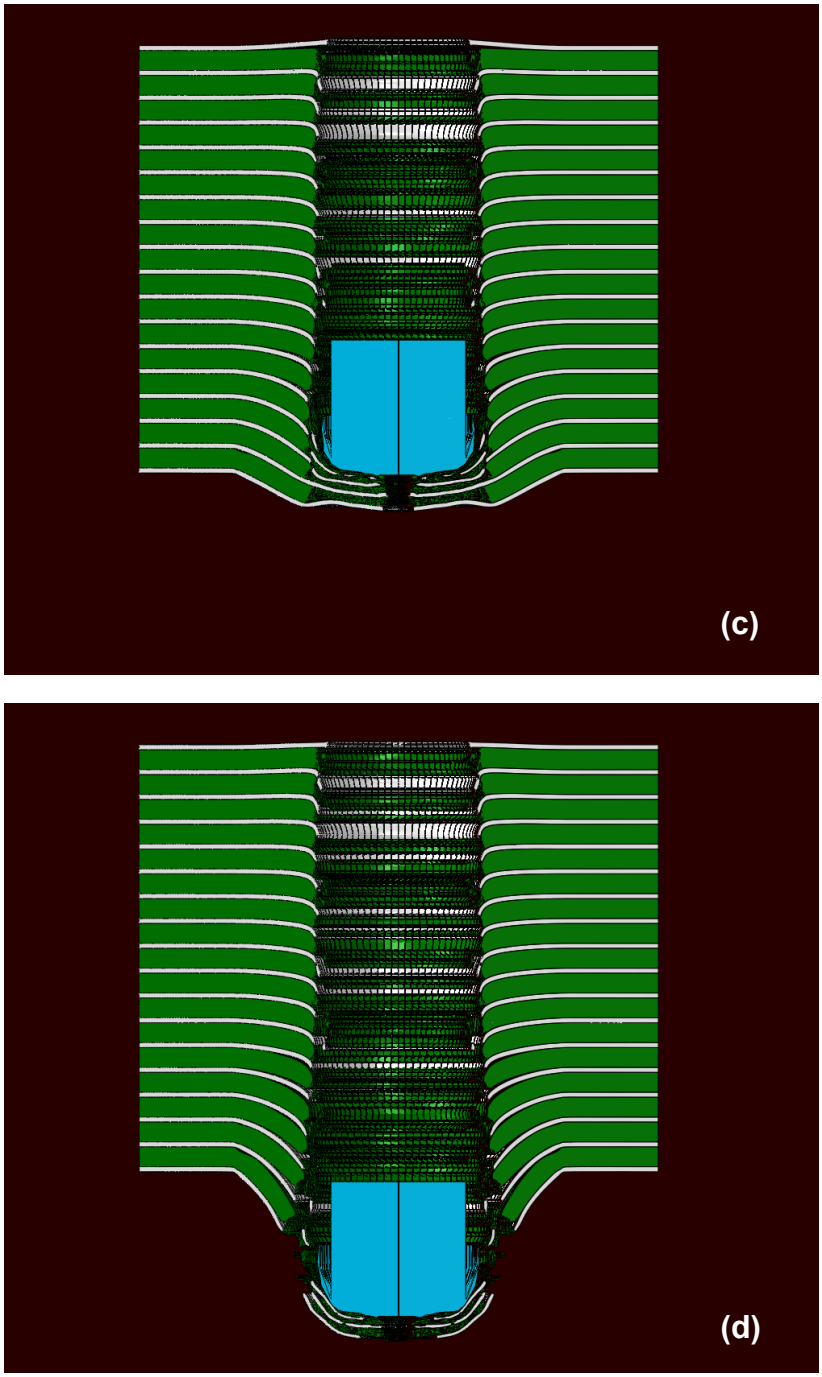

Figure 10. Continued.

(e) The line density of the cracks within the target plate was monitored as a function of the FSP penetration depth, by employing an in-house developed post-processing program. This analysis reveals that, as expected, initially the rate of crack linear density increases gradually with the FSP penetration depth (since target plate damage is dominated by the $TiAl_3$-borne cracks). However, once delamination beings to take place, the rate of crack linear density increase becomes quite high and peaks at the instant when the projectile exits the target plate;

(f) Examination of the MILC target-plate region surrounding the penetration hole reveals that the material located in this region has experienced a substantial amount of plastic deformation and

damage. This finding suggests that the Ti/$TiAl_3$ MILC in question should possess a good ballistic-penetration resistance. Simply stated, energy required for plastic deformation and fracture/delamination is supplied by the projectile through reduction of its kinetic energy. Hence, the larger is the extent of energy consumption for plastic deformation and damage, the more efficient will be the defeat of the projectile. This was confirmed in the present work by showing that the reduction in the FSP tail speed correlates quite well with the target-plate crack linear density; and

(g) The region of the FSP bordering its front face has undergone significant plastic deformation (mushrooming). This finding is expected since: (i) the high stresses within the projectile are localized in the region adjacent to its front face; and (ii) dissipation of the work of plastic deformation in this region results in local heating and thermal softening of the FSP material, facilitating its plastic deformation.

4.4. Suitability of Ti/$TiAl_3$ MILCs for Use in Ballistic-Armor Applications

Ti/$TiAl_3$ MILCs investigated in the present work are considered as candidate materials for use in light multi-functional, multi-layer armor applications. While ballistic armor can be classified in several different ways, within one of the classification, ballistic armor is divided into the so-called structural and appliqué *add-on* armor. Both classes of armor are required to provide the necessary level of ballistic protection in a mass efficient manner. However, the structural armor is additionally required to withstand structural loading without degradation and failure. For example, in the case of military vehicles, the structural armor must withstand the loads generated at the wheels/ground surfaces and propagated into the vehicle structure. Typically, structural armor is an integral part of the vehicle, i.e. structural armor panels are used in the construction of the vehicle body. In this case, as mentioned earlier, the armor is of a multi-layer character and the Ti/$TiAl_3$ MILC panels would act both as structural panels and as backup plates for the ceramic hard face. In the case of the add-on armor, the armored structure is attached (via velcro-type connectors and/or adhesives) to the vehicle structure. Since the interface between the appliqué armor and the vehicle structure is of a compliant character, this interface isolates, mechanically, the hard and brittle components of the appliqué armor from the vehicle structural loads. Due to these differences in some of the functional requirements and the vehicle/armor integration, one may expect some variation in the properties/performance requirements in order for the materials to be used in structural and add-on armor applications. Consequently, a candidate material like Ti/$TiAl_3$ MILCs may be more suited for one of the two classes (i.e. structural vs. add-on) of ballistic armor.

In the case of the structural armor, considering the fact that the armor is used in the construction of the vehicle cabin/hull itself, in addition to stopping the incoming FSP without penetration, the armor should ensure that backface spalling (which generates high kinetic energy fragments) is not extensive, in the case of incomplete penetration. While the main role of the innermost layer (made of a phenolic-resin based material) of the structural armor is to act as a spall-catcher, excessive spall formation can overwhelm this layer. Consequently, to assess the potential of Ti/$TiAl_3$ MILCs for use in structural-armor applications, two figures of merit are identified and quantified:

(a) V_{50}—a measure of the ballistic-protection performance offered by an armor solution, defined as the incident projectile velocity at which the probability of armor penetration is 50%. To determine V_{50}, the conventional *six-round limit* experimental procedure is mimicked, computationally, in the present work. Within this procedure: (a) one fresh FSP is used to impact one fresh target plate; (b) the procedure is repeated by increasing the FSP incident velocity in small increments; and (c) each

impact test is considered to be a separate statistical event and, consequently, V_{50} is obtained by averaging the three highest velocities at which partial penetrations take place and the three lowest velocities at which complete penetrations take place. The results of this procedure are depicted in Figure 11(a). For comparison, the V_{50} results for the cases of the AA2139 aluminum armor [34], MIL A46100 steel armor [35] and S2 glass-reinforced polyvinyl ester epoxy composite armor [2], all at the same level of areal density as the Ti/$TiAl_3$ MILC armor, are also depicted in Figure 11(a). For convenience, the results are normalized by V_{50} for the Ti/$TiAl_3$ MILC armor. The results displayed in Figure 11(a) indicate that, with respect to V_{50}, Ti/$TiAl_3$ MILC armor outperforms the other three alternatives; and

(b) the maximum relative momentum transferred to the witness plate—Figure 11(b) shows the computed results pertaining to the momentum transfer by the high kinetic-energy armor fragments to the witness plate. For convenience, the results are normalized by the momentum acquired by the witness plate in the case of the Ti/$TiAl_3$ MILC armor. Examination of the results shown in Figure 11(b) reveals that the performance of the Ti/$TiAl_3$ armor, in this case, is comparable to that of the polymer-matrix composite armor, but inferior to the other two armored structures. This finding appears to suggest that Ti/$TiAl_3$ MILC armor may not be a suitable candidate for use in structural armor applications. However, close examination of the material distribution during penetration of the Ti/$TiAl_3$ MILC target-plate by the FSP, revealed that a majority of the momentum transferred to the witness plate was associated with the innermost Ti layer. In other words, this layer contained loose $TiAl_3$ fragments and acted as an auxiliary spall-catcher. Thus, based on the results presented in Figure 11(b), Ti/$TiAl_3$ MILC cannot be excluded as a potential structural-armor material. Unfortunately, Ti/$TiAl_3$ MILC contains the low toughness $TiAl_3$ phase which may crack under in-service structural loads. On this basis, one can eliminate Ti/$TiAl_3$ MILC for use in structural armor applications.

In the case of the add-on armor, excessive generation of the spall fragments is not generally expected to be a major shortcoming for the prospective armor material. The main reason is that the appliqué armor is attached to the cabin/vehicle-hull walls and thus, separated from the cabin interior. Consequently, not only the spall-catcher but also the cabin/vehicle-hull walls would act to prevent the ingress of high-velocity spall fragments into the vehicle interior. Also, as mentioned above, in-service structural loads are not expected to propagate into the appliqué armor and, hence, limited toughness of a material layer within the armor may not be a serious shortcoming. These two observations suggest that Ti/$TiAl_3$ MILCs should not be *a priori* excluded as potential add-on armor materials. In the case of the appliqué armor, the ballistic protection performance is commonly judged using the so-called mass efficiency. This metric is defined as:

$$e_m = \frac{(p_o - p)\rho_{structure}}{T_{armor}\rho_{armor}} \tag{29}$$

where p_0 and p are the penetration distances into the metal structure by the projectile in the absence, and presence, of the (add-on) armor, respectively, ρ is the mass density, T is the thickness and subscripts *structure* and *armor* are self-explanatory. It should be noted that the denominator in Eq. (29) represents the areal density of the add-on armor. To determine e_m, in the present work, a thick structural plate made of MIL A46100 was attached to the backface of the armor and the FSP incident velocity was set to a value exceeding V_{50}. The results yielded by this analysis are depicted in Figure

11(c). Examination of the results shown in Figure 11(c) reveals that, as expected, e_m for MIL A46100 is 1.0. In this case, since the structural plate and the add-on armor are made of the same material, reduction in the structural-plate penetration due to application of the armor is equal to the armor thickness. More importantly, it is seen that $Ti/TiAl_3$ MILC armor possesses the highest level of mass efficiency among the four candidate armor materials. Thus, $Ti/TiAl_3$ MILC armor appears to be a suitable and, potentially, high-performance candidate material for use in the add-on armor applications.

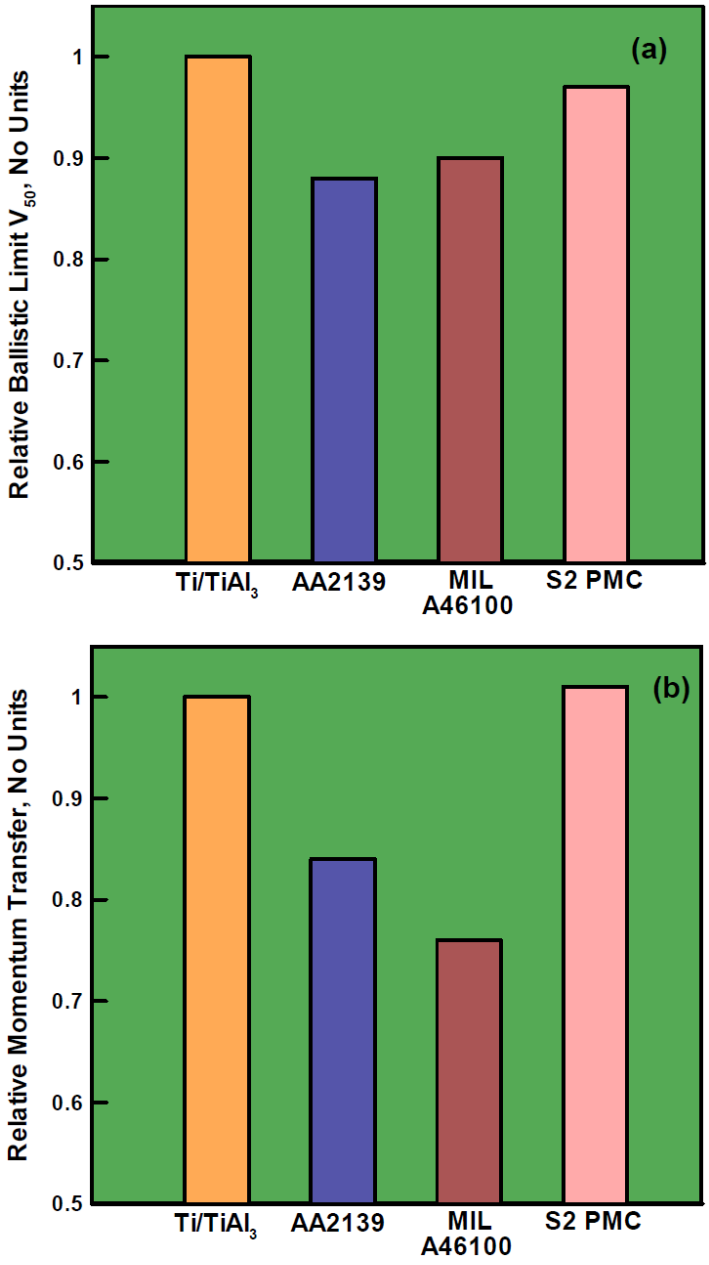

Figure 11. Suitability analysis of $Ti/TiAl_3$ MILCs for use in structural and add-on armor applications: (a) relative V_{50}, a measure of the ballistic limit; (b) relative momentum transfer to the witness plate; and (c) mass efficiency. Three armor materials are examined as alternatives: (i) AA2139 aluminum [34]; (ii) MIL A46100 steel [35]; and (iii) S2 glass-reinforced polyvinyl ester epoxy composite [2].

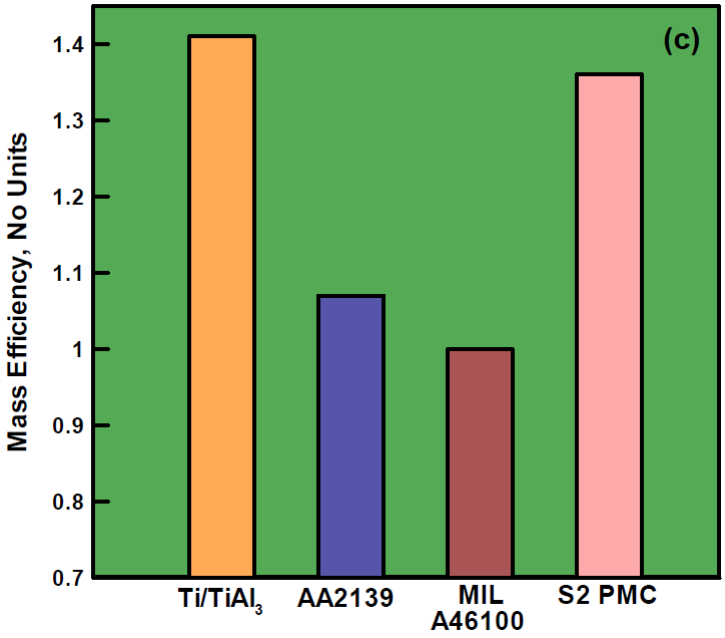

Figure 11. Continued.

5. Conclusion

Based on the results obtained in the present work, the following main summary remarks and conclusions can be drawn:

1. A purely computational approach has been developed to help establish suitability of $Ti/TiAl_3$ metal/intermetallic laminated composites (MILCs) for use in light-armor applications, as comprehensive experimental data are not available. This computational approach is based on a transient, nonlinear-dynamics, finite-element model and analysis of a $Ti/TiAl_3$ MILC target plate impacted normally, over a range of incident velocities, by a fragment simulating projectile (FSP).

2. In order to model the delamination and spallation of the target plate during ballistic impact, $Ti/TiAl_3$ decohesion potentials must be known. They were derived and parameterized using atomic-scale calculations.

3. By analyzing evolution and distribution of the deformation and damage of the target plate and by correlating the results of this analysis with the evolution of the projectile velocity/kinetic energy, the $Ti/TiAl_3$ MILCs were shown to have a superior ballistic limit. However, these materials were also shown to have limited fracture toughness (required in structural armor applications).

4. A comparison of figures of merit for the subject material and three alternative materials indicated that $Ti/TiAl_3$ MILCs could be considered as viable candidate materials in add-on, but not in structural, armor applications.

Acknowledgements

This material is based upon research supported by the Office of Naval Research under Award Number N00014-14-1-0286, "Reactive-Moiety Functionalization of Polyurea for Increased Shock-Mitigation Performance." The authors are indebted to Dr. Roshdy Barsoum of ONR for his continuing support and interest in the present work.

Conflict of Interest

The authors declare no conflicts of interest regarding this paper.

References

1. Grujicic M, Pandurangan B, d'Entremont BP, et al. (2012) The role of adhesive in the ballistic/structural performance of ceramic/polymer-matrix composite hybrid armor. *Mater Des* 41: 380–393.
2. Grujicic M, Pandurangan B, Zecevic U, et al. (2007) Ballistic performance of alumina/S-2 glass-reinforced polymer-matrix composite hybrid lightweight armor against armor piercing (AP) and non-AP projectiles. *Multidisc Model Mater Struct* 3: 287–312.
3. Medvedovski E (2002) Alumina ceramics for ballistic protection. *Am Ceram Soc Bull* 81: 27–32.
4. Aghajanian MK, Morgan BN, Singh JR, et al. (2001) A new family of reaction bonded ceramics for armor applications. In: *Proceedings of PAC RIM 4*, Maui. Hawaii, Paper No. PAC6-H-04-2001.
5. Grujicic M, Glomski PS, He T, et al. (2009) Material modeling and ballistic-resistance analysis of armor-grade composites reinforced with high-performance fibers. *J Mater Eng Perform* 18: 1169–1182.
6. Grujicic M, Pandurangan B, Snipes JS, et al. (2013) Multi-length scale enriched continuum-level material model for Kevlar®-fiber reinforced polymer-matrix composites. *J Mater Eng Perform* 22: 681–695.
7. Grujicic M, Bell WC, Biggers SB, et al. (2008) Enhancement of the ballistic-protection performance of E-glass reinforced poly-vinyl-ester-epoxy composite armor via the use of a carbon-nanotube forest-mat strike face. *J Mater: Des Appl* 222: 15–28.
8. Grujicic M, Bell WC, Pandurangan B, et al. (2011) Computational investigation of structured shocks in Al/SiC-particulates metal matrix composites. *Multidisc Model Mater Struct* 7: 469–497.
9. Cheeseman BA, Jensen R, Hopped C (2005), *Protecting the Future Force: Advanced Materials and Analysis Enable Robust Composite Armor.* The AMPTIAC Quarterly, 8: 37–43.
10. Vecchio KS (2005) Synthetic multifunctional metallic-intermetallic laminate composites. *J Metals* 57: 25–31.
11. Price RD, Jiang F, Kulin RM, et al. (2011) Effects of ductile phase volume fraction on the mechanical properties of Ti–Al_3Ti metal-intermetallic laminate (MIL) composites. *Mater Sci Eng A* 528: 3134–3146.
12. Yang C, Guo C, Zhu S, et al. (2015) Fracture behavior of Ti/Al_3Ti metal-intermetallic laminate (MIL) composite under dynamic loading. *Mater Sci Eng A* 637: 235–242.
13. Lazurenko DV, Mali VI, Bataev IA, et al. (2015) Metal-intermetallic laminate Ti-Al_3Ti composites produced by spark plasma sintering of titanium and aluminum foils enclosed in titanium shells. *Metall Mater Trans A* 46A: 4326–4334.
14. Cao Y, Zhu S, Guo C, et al. (2015) Numerical investigation of the ballistic performance of metal-intermetallic laminate composites. *Adv Compos Mater* 22: 437–456.
15. Yu H, Lu C, Tieu AK, et al. (2016) Annealing effect on microstructure and mechanical properties of Al/Ti/Al laminate sheets. *Mater Sci Eng A* 20: 195–204.
16. Harach DJ (2000) *Processing, properties, and ballistic performance of Ti-Al_3Ti Metal-Intermetallic Laminate (MIL) composites.* PhD Thesis, University of California, San Diego, CA.

17. Zelepugin S, Mali V, Zelepugin A, et al. (2012), Failure of metallic-intermetallic laminate composites under dynamic loading. *AIP Conference Proceedings* 1426: 1101.
18. ABAQUS Version 6.13, User Documentation, Dassault Systèmes, 2013.
19. Grujicic M, d'Entremont BP, Pandurangan B, et al. (2012) A study of the blast-induced brain white-matter damage and the associated diffuse axonal injury. *Multidisc Model Mater Struct* 8: 213–245.
20. Grujicic M, Bell WC, Pandurangan B, et al. (2012) Inclusion of material nonlinearity and inelasticity into a continuum-level material model for soda-lime glass. *Mater Des* 35: 144–155.
21. Grujicic M, Bell WC, Pandurangan B, et al. (2012) Effect of the tin- vs. air-side plate-glass orientation on the impact response and penetration resistance of a laminated transparent-armor structure. *J Mater Des Appl* 226: 119–143.
22. Grujicic M, Pandurangan B, Bell WC, et al. (2012) Shock-wave attenuation and energy-dissipation potential of granular materials. *J Mater Eng Perform* 21: 167–179.
23. Grujicic M, Pandurangan B, Bell WC, et al. (2011) Molecular-level simulations of shock generation and propagation in polyurea. *Mater Sci Eng A* 528: 3799–3808.
24. Johnson GR, Cook WH (1983) A constitutive model and data for metals subjected to large strains, high strain rates and high temperatures. In: *Proceedings of the 7th International Symposium on Ballistics*, the Netherlands, Arlington, VA: American Defense Preparedness Association.
25. AUTODYN-2D and 3D, Version 6.1, User Documentation, Century Dynamics Inc., 2006.
26. Johnson GR, Holmquist TJ (1994) An improved computational constitutive model for brittle materials, in *AIP Conference Proceedings, Colorado Springs, CO 1993*, American Institute of Physics, Melville, NY, 309: 981–984.
27. Li T, Grignon F, Benson D, et al. (2004) Modeling the elastic properties and damage evolution in Ti–Al_3Ti metal–intermetallic laminate (MIL) composites. *Mater Sci Eng A* 374: 10–26.
28. Needleman A (1987) A continuum model for void nucleation by inclusion debonding. *J Appl Mech* 54: 525–531.
29. Socrate S (1995) *Mechanics of microvoid nucleation and growth in high-strength metastable austenitic steels.* PhD Thesis, Massachusetts Institute of Technology, Cambridge, MA.
30. Grujicic M, Dang P (1996) Atomic-scale analysis of martensitic transformation in titanium with vanadium – Part I: Verification of the EAM potential. *Mater Sci Eng A* 205: 139–152.
31. Dang P, Grujicic M (1997) Transformation toughening in the Gamma TiAl/Beta Ti-V system – Part II: A molecular dynamics analysis. *J Mater Sci* 32: 4875–4887.
32. Grujicic M, Olson GB, Owen WS (1985) Mobility of the β1-γ1' martensitic interface in Cu-Al-Ni. I. Experimental measurements. *Metall Trans A* 16: 1723–1734.
33. Grujicic M, Olson GB, Owen WS (1985) Mobility of the β1-γ1' martensitic interface in Cu-Al-Ni. II. Model calculations. *Metall Trans A* 16: 1735–1744.
34. Grujicic M, Arakere G, Yen C-F, et al. (2011) Computational investigation of hardness evolution during friction-stir welding of AA5083 and AA2139 aluminum alloys. *J Mater Eng Perform* 20: 1097–1108.
35. Grujicic M, Ramaswami S, Snipes JS, et al. (2013) Multi-physics modeling and simulations of MIL A46100 armor-grade martensitic steel gas metal arc welding process. *J Mater Eng Perform* 22: 2950–2969.

AIMS Press

© 2016 S. Ramaswami, et al., licensee AIMS Press. This is an open access article distributed under the terms of the Creative Commons Attribution License (http://creativecommons.org/licenses/by/4.0)